Energy & Environmental Science

Cite this: *Energy Environ. Sci.*, 2012, **5**, 6521

www.rsc.org/ees

PAPER

Investigation of the degradation mechanisms of a variety of organic photovoltaic devices by combination of imaging techniques—the ISOS-3 inter-laboratory collaboration†

Roland Rösch,[a] David M. Tanenbaum,[bc] Mikkel Jørgensen,[b] Marco Seeland,[a] Maik Bärenklau,[a] Martin Hermenau,[d] Eszter Voroshazi,[ef] Matthew T. Lloyd,[g] Yulia Galagan,[h] Birger Zimmermann,[i] Uli Würfel,[i] Markus Hösel,[b] Henrik F. Dam,[b] Suren A. Gevorgyan,[b] Suleyman Kudret,[j] Wouter Maes,[j] Laurence Lutsen,[k] Dirk Vanderzande,[j] Ronn Andriessen,[h] Gerardo Teran-Escobar,[l] Monica Lira-Cantu,[l] Agnès Rivaton,[mn] Gülşah Y. Uzunoğlu,[o] David Germack,[p] Birgitta Andreasen,[b] Morten V. Madsen,[b] Kion Norrman,[b] Harald Hoppe*[a] and Frederik C. Krebs[b]

Received 20th December 2011, Accepted 24th January 2012
DOI: 10.1039/c2ee03508a

The investigation of degradation of seven distinct sets (with a number of individual cells of $n \geq 12$) of state of the art organic photovoltaic devices prepared by leading research laboratories with a combination of imaging methods is reported. All devices have been shipped to and degraded at Risø DTU up to 1830 hours in accordance with established ISOS-3 protocols under defined illumination conditions. Imaging of device function at different stages of degradation was performed by laser-beam induced current (LBIC) scanning; luminescence imaging, specifically photoluminescence (PLI) and electroluminescence (ELI); as well as by lock-in thermography (LIT). Each of the imaging techniques exhibits its specific advantages with respect to sensing certain degradation features, which will be compared and discussed here in detail. As a consequence, a combination of several imaging techniques yields very conclusive information about the degradation processes controlling device function. The large variety of device architectures in turn enables valuable progress in the proper interpretation of imaging results—hence revealing the benefits of this large scale cooperation in making a step forward in the understanding of organic solar cell aging and its interpretation by state-of-the-art imaging methods.

1. Introduction

To date organic photovoltaics (OPV)[1–4] is steadily maturing towards a commercially viable technology.[5] This market entry opportunity is on the one hand driven by the impressive progress demonstrated by increasing the power conversion efficiency (PCE) of solar cell devices towards 8–10% within the last decade.[6,7] On the other hand, device stability and lifetime is a key factor allowing the launch of products beyond the scope of gadgets. Hence recently more consolidated efforts in

[a]*Institute of Physics, Ilmenau University of Technology, Weimarer Str. 32, 98693 Ilmenau, Germany. E-mail: harald.hoppe@tu-ilmenau.de*
[b]*Department of Energy Conversion and Storage, Technical University of Denmark, Frederiksborgvej 399, DK-4000 Roskilde, Denmark*
[c]*Department of Physics and Astronomy, Pomona College, Claremont, CA, 91711, USA*
[d]*Arbeitsgruppe Organische Solarzellen (OSOL), Institut für Angewandte Photophysik, Technische Universität Dresden, 01062 Dresden, Germany*
[e]*Imec, Kapeldreef 75, 3000 Leuven, Belgium*
[f]*Katholieke Universiteit Leuven, ESAT, Kasteelpark Arenberg 10, 3000 Leuven, Belgium*
[g]*National Renewable Energy Laboratory, Golden, CO, 80401, USA*
[h]*Holst Centre, High Tech Campus 31, 5656 AE Eindhoven, The Netherlands*
[i]*Fraunhofer Institute for Solar Energy Systems ISE, Heidenhofstrasse 2, D-79110 Freiburg, Germany*
[j]*Hasselt University, Campus, Agoralaan 1, Building D, WET/OBPC, B-3590 Diepenbeek, Belgium*
[k]*IMEC, IMOMEC associated laboratory, Campus University of Hasselt, Wetenscharpspark 1, B-3590 Diepenbeek, Belgium*
[l]*Centre d'Investigació en Nanociència i Nanotecnologia (CIN2, CSIC), Laboratory of Nanostructured Materials for Photovoltaic Energy, ETSE, Campus UAB, Edifici Q, 2nd Floor, E-08193 Bellaterra (Barcelona), Spain*
[m]*Clermont Université, Université Blaise Pascal, Laboratorie de Photochimie Moléculaire et Macromoléculaire (LPMM), BP10448 Clermont-Ferrand, France*
[n]*CNRS, UMR6505, LPMM, F-63177 Aubiére, France*
[o]*TÜBITAK National Metrology Institute (UME), Photonic and Electronic Sensors Laboratory, P.O. Box 54, 41470 Gebze, Kocaeli, Turkey*
[p]*Condensed Matter Physics, Brookhaven National Lab, Building 510B, Upton, NY, 11973, USA*

† Electronic supplementary information (ESI) available. See DOI: 10.1039/c2ee03508a

research and development are directed towards improvements in device stability by the understanding of acting degradation processes and developing of countermeasures and constructive improvements within the device architecture.[8–12] The third pillar for commercialization of OPV is a scalable roll-to-roll compatible processing technology that can yield potentially very cost effective products in the highly competitive field of power generation from harvesting of solar energy.[4,13] Due to the fact that OPV technology is at the edge of entering the market, reliable characterization and standardization of device stability reporting is a basic necessity. Fruitful discussions among scientists from research and development at the three International Summits on Organic Photovoltaic Stability (ISOS-1, ISOS-2 and ISOS-3) have therefore generated an agreement concerning the testing conditions and proper reporting of OPV device stability data.[14]

This report is part of a series of publications resulting from specific research collaborations established at the Third International Summit on Organic Photovoltaic Stability (ISOS-3), aiming for advanced understanding and improved and comparable characterization of OPV degradation. Seven distinct sets of devices produced at different laboratories were aged under various conditions at Risø DTU: accelerated full sun simulation; low level indoor fluorescent lighting; and dark storage with daily measurement under full sun simulation.[15] While the first report summarizes the overall degradation behavior of these devices by efficiency data *versus* stress time, more specific investigations done during the course of these experiments are the subject of the remaining reports. As time dependent efficiency data or *IV*-characteristics alone cannot reveal the precise origins of failure of these devices, lateral and local investigation methods were applied in order to obtain a more thorough understanding of the underlying degradation mechanisms. This report is making a step from global device behavior to local—or more precisely—spatially resolved degradation by the application of a set of imaging characterization methods. Imaging methods employed within this study are laser-beam induced current (LBIC), dark lock-in thermography (DLIT), electroluminescence (ELI) and photoluminescence (PLI) imaging.

Due to the non-destructive nature of the imaging characterization, one and the same device was repeatedly aged under accelerated full sun simulation and repeatedly imaged within this experiment. This procedure leads to the important advantage that the degradation patterns obtained after various stress times can be compared directly. In conclusion, the aim of this experiment was to connect *IV*-characteristics and imaging data to learn about the predominant factors causing failure of the devices. It is noteworthy that the knowledge of the exact layer structure of the devices is explicitly required for a meaningful interpretation of the collected imaging data. Therefore important details of the device structure will be mentioned herein, however, the full information on all device structures is detailed within the first report.[15]

In brief, imaging characterization has been applied as a tool to investigate degradation of OPV devices only rarely in the past. The most widespread and for longer time applied technique is LBIC,[10,16,17] but also luminescence imaging (ELI and PLI) and dark lock-in thermography (DLIT) have proven their applicability to clarify device degradation, recently.[11,12] A review on the application of imaging methods in OPV degradation studies is published elsewhere.[18]

2. Experimental

2.1 Device preparation and material system

All photovoltaic devices were prepared by various collaborators within the consortium according to the round robin discussion group and planning at the ISOS-3 workshop. The devices were prepared by six different groups: the Institute of Applied Photophysics in Dresden, Germany (IAPP), the imec in Leuven, Belgium (IMEC), the National Renewable Energy Laboratory in Golden, Colorado (NREL), the Holst centre in Eindhoven, The Netherlands (HOLST), the Fraunhofer Institute for Solar Energy Systems in Freiburg, Germany (ISE) and the Risø National Laboratory for Sustainable Energy, Denmark Technical University in Roskilde, Denmark (Risø). Fig. 1 displays all investigated devices true to scale.

The details of the preparation and architecture of the photovoltaic devices investigated within this collaboration can be found within the first article of this series.[15] In brief, all devices utilize the bulk heterojunction architecture for the photoactive layer. The material system in the case of vacuum processing was based on zinc-phthalocyanine:fullerene ($ZnPc:C_{60}$), in all other cases it was based on P3HT:PCBM (poly(3-hexylthiophen-2,5-

Broader context

We report about a collaborative effort on the investigation of the main degradation mechanisms of state-of-the-art organic and polymer solar cells by accelerated lifetime tests and means of imaging techniques. The study is a part of the ISOS-3 collaboration, established during the Third International Summit on Organic Solar Cell Stability, devoted to discovering organic solar cell degradation by accelerated lifetime tests, imaging techniques, *in situ* external quantum efficiency measurements and chemical profiling by secondary ion mass spectroscopy. Due to the broad experimental approach and various device architectures investigated within this collaboration, the results and conclusions are not only valid for these particular devices, but also should provide valuable information for the whole community dedicated to organic solar cell research and development. In this paper improved understanding of different degradation routes revealed by advanced imaging techniques, namely luminescence imaging, lock-in thermography and light beam induced current is presented in combination with *IV*-characteristics. One main conclusion is that the stability of to-dates organic photovoltaic devices remains mostly limited by electrode degradation, whereas the intrinsic degradation of the organic photoactive layer plays only a minor role. Thus this work provides guidelines for future improvements of stable solar cell device operation.

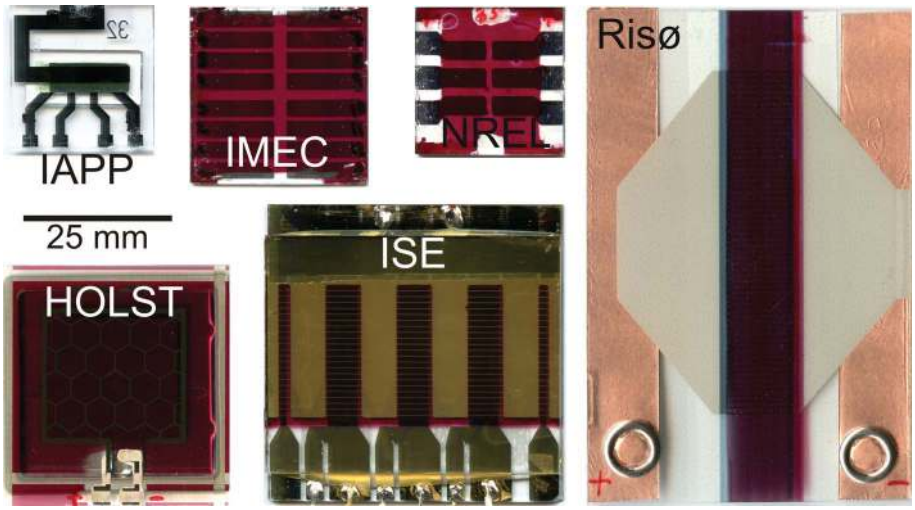

Fig. 1 True to scale overview on all device structures investigated within this study.

diyl):phenyl-C61-butyric acid methyl ester) or P3HT-*co*-P3AcET:PCBM processed from solution.[15] A larger variation occurred in the application of electron transport/hole blocking and hole transport/electron blocking layers, as well as in electrode materials and structures. Five of the devices were processed on glass and two on flexible PET-substrates. Whereas the flexible devices were protected by barrier sealing including an UV-filter, only some of the devices processed on glass were sealed under glass or stainless steel. Overall, seven distinctively different device architectures were used and large variations in the cell size, its architecture and the fabrication process form the experimental basis for improving the fundamental understanding about various degradation processes and the applicability of complementary imaging methods.

2.2 Degradation/aging conditions

The details about the degradation conditions are described in the first article within this series.[15] In brief, three different illumination conditions were applied in combination with periodic *IV*-characterization of the devices: accelerated full sun simulation; low level indoor fluorescent lighting; and dark storage with daily measurement under full sun simulation. The atmosphere was ambient and uncontrolled in all cases. The different aging conditions yielded not only widely varied stress levels of illumination intensities but also correlated thermal stress as well as photocurrent fluxes passing through the device. Whereas the fluorescent light as well as the dark storage took place at approximately room temperature, full sun illumination under a solar simulator caused temperatures of up to 85 °C as measured by a thermocouple on the outer backside of the cells. Therefore the inner temperature of the cells, especially of the photoactive layer and the electrodes could be even higher, potentially exceeding 100 °C. After certain times devices were removed from the stress condition and investigated by various non-destructive or destructive characterization methods. In this report only the most severe stress condition, namely full sun illumination, is considered for analysis by non-destructive imaging investigation.

2.3 Laser-beam induced current (LBIC)

The measurement principle of laser-beam induced current (LBIC) is based on point-by-point scanning of a focused monochromatic light beam ($\lambda = 410$ nm, $P = 5$ mW) with typical beam diameters of 100 μm across the active area of the device, which limits also the spatial resolution to ~100 μm. To be able to detect the small locally generated photocurrent, the solar cell is usually held under short-circuit conditions and the excitation light is usually modulated by a frequency, allowing precise photocurrent detection by the lock-in technique.[19] However, no lock-in technique was used within this study. By simultaneous registration of the spatial position of the light-spot on the device, the LBIC image is collected and constructed by a computer. Darker regions in the LBIC image thus correspond to smaller photocurrents, which have to be correlated with the local device degradation. As the generation of LBIC images requires light absorption, current generation and extraction, this technique monitors the complete device functioning at locally high but globally low excitation levels. Although high light intensities of more than 50 W cm^{-2} corresponding to 500 suns are reached, no negative impact on the active layer is expected due to the fact that each point is exposed to the laser beam for only less than 1 μs. An equal energy dose is deposited under one sun during 0.5 ms and therefore not supposed to be harmful. The experimental setup for performing LBIC measurements is depicted in Fig. 2.

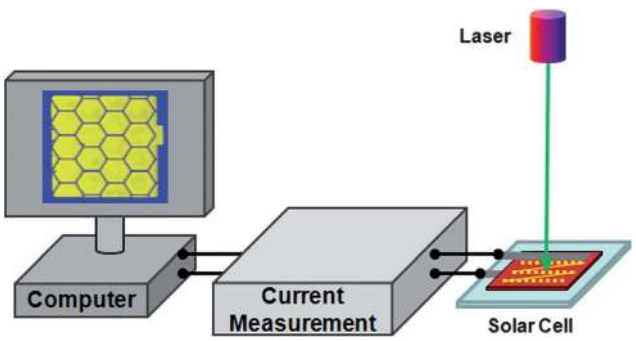

Fig. 2 Schematic of a LBIC measurement setup.

2.4 Luminescence imaging

Luminescence imaging makes use of the capability of the organic semiconductor or the respective heterojunction to yield radiative de-excitation processes. This method yields the complete image of the device at once, possibly enabling very fast characterization. The challenge lies in the quantitative detection of the generally very weak luminescence signals arising from organic solar cells, which are orders of magnitude lower than those for organic light emitting diode (OLED) devices. The experimental setup for performing luminescence imaging is displayed in Fig. 4a. The charge coupled device silicon detector and the optics used allow resolving spatial features down to ~10 μm, depending on the sample size.

2.4.1 Photoluminescence imaging (PLI). In photoluminescence imaging the whole device is homogeneously illuminated by a sufficiently powerful light-source with spectral distribution matching the active layer absorption, *e.g.* light emitting diodes. Electrons within pristine phases of the donor or acceptor semiconductor are lifted into an excited state (HOMO–LUMO transition), followed by de-excitation upon radiative recombination within one and the same material. This process is generally named photoluminescence. In order to detect only the light emitted from the semiconductor, a cut-off filter is placed in front of a sensitive camera, *e.g.* a charge coupled device (CCD) silicon detector. Fig. 3 displays the transmission- and photoluminescence spectrum of P3HT:PCBM, the luminescence spectrum of the light-source and the transmission spectrum of the cut-off filter. The luminosity of the light-source is about 0.1 W, and it is used to illuminate an area of approximately 0.1 m^2. This equals 0.001 suns intensity and is therefore harmless for the photoactive layer. As the photoluminescence arising from photoactive layers is strongly depending on the bulk heterojunction morphology, this technique potentially yields information about the homogeneity of the active layer processing. As solar cells are designed in such a way that photoinduced charge transfer is maximized and photoluminescence is minimized, even at careful choices of the light excitation source and the blocking filter, reflected excitation light is in competition with the true photoluminescence signal.[18]

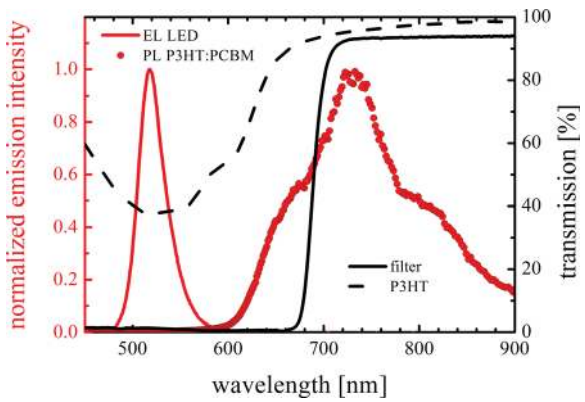

Fig. 3 Photoluminescence (PL) emission spectra of a P3HT:PCBM based polymer solar cell (red dots). For imaging applications, the PL can be generated using a light-emitting diode (LED) excitation (red line) within the absorption range of the polymer (dashed black line). The excitation light is blocked in front of the CCD using the transmission (black line) of a cut-off filter.

2.4.2 Electroluminescence imaging (ELI). For emission of electroluminescence the solar cell device is driven by a DC forward bias voltage of typically 1.5 V, yielding electrons injected from the cathode and holes injected from the anode. A minor fraction of these charge carriers can recombine radiatively within percolating pristine phases or across the semiconductor heterojunction. The latter process involves so-called charge transfer complexes (CTC) between holes in the donor and electrons in the acceptor.[20,21] As the current is driven through the total solar cell, series resistance effects control the lateral electroluminescence emission pattern depending on the point of device operation.[22] Since electroluminescence requires locally functioning electrode–active layer interfaces, it constitutes a good method to test this sensitive part of the device. Hereafter we will mostly refer to "electrode delamination" as the *terminus technicus*, which shall be a general term not only for literal delamination, but also shall include effects such as blocking layer formation due to local oxidation of the electrode at the interface to the active layer and others as well.

2.5 Lock-in thermography (LIT)

Lock-in thermography is a highly sensitive method for detection of local device heating upon excitation.[23] Excitation can be either done with illumination (illuminated lock-in thermography—ILIT) or by current injection (dark lock-in thermography—DLIT). The lock-in principle allows detection of temperature differences below the milli-Kelvin (mK) range. However, it requires a periodically applied excitation, hence a function generator in combination with an amplifier is used to generate either AC light emission or electric currents to drive the device at proper frequencies. For sensing of the local heating, a high-frequency computer controlled infrared (IR) camera is employed, which images the whole device simultaneously. A schematic of the LIT-measurement setup is shown in Fig. 4b. In general, the two modes of lock-in thermography can be compared with those of luminescence imaging, with the difference that no visible light emission, but rather heat radiation is imaged. This especially enables the detection of shunts in the device that generally cannot be detected by luminescence imaging. In this experiment only dark lock-in thermography was applied for analysis with a typical excitation of about 1.5 V to 2 V and a modulation frequency of 10 Hz. Depending on the observed area, features down to 15 μm can be resolved.

2.6 Cycle experiment

Due to the fact that all of these imaging methods allow for non-destructive device testing a special cycle experiment has been performed as part of the overall degradation investigation: after an initial investigation by all imaging methods and standard device characterization, one and the same device was aged under full sun simulation for various exposure times; then the solar cell was removed from the degradation setup and characterized by all the imaging methods as well as by external quantum efficiency

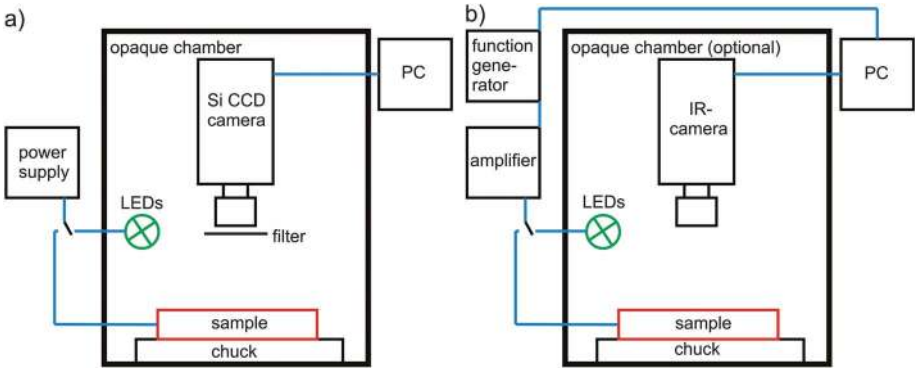

Fig. 4 Experimental setup of luminescence imaging (a) and lock-in thermography (b).

measurements again; after that the device returned to the degradation setup for continued degradation, followed by another non-destructive investigation. This procedure allowed following the formation of specific degradation patterns of selected devices with exposure time under the degradation setup. As a consequence an improved correlation between ageing and features visible by the imaging methods was achieved. The course of action for the cycle experiment is depicted in Fig. 5 in the form of a flow chart.

3. Results and discussion

The application of various imaging techniques within this photovoltaic device degradation study yielded not only lateral resolved information about device function at different stages of degradation, but also improved by far—and beyond any straight forward analysis of simple *IV*-characteristics—the understanding of the actual degradation process taking place within the devices. In fact, some of the degradation processes could be revealed by combining the information from *IV*-characteristics and a single imaging technique. However, more peculiar degradation patterns could only be "decoded", when the information from several imaging techniques were viewed in combination. However, not in all cases imaging could provide unambiguous information, and common knowledge about degradation processes was consulted in general.

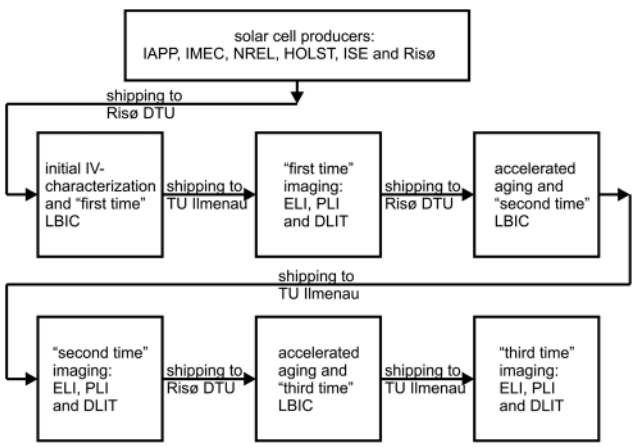

Fig. 5 Course of action for the cycle experiment.

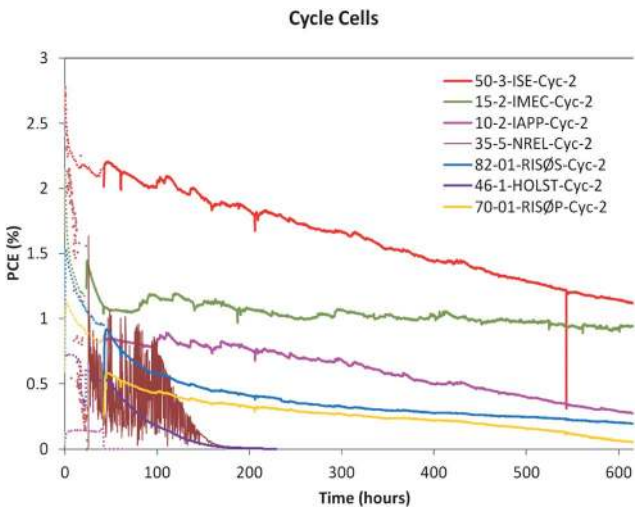

Fig. 6 Degradation data of all solar cells investigated in the cycle experiment under full sun illumination and up to 85 °C accelerated stress conditions. The dotted lines represent the accelerated aging between the first and second time imaging, while the solid lines indicate the accelerated ageing between the second and third time imaging. Roughly the solar cells can be sorted into three different groups: (i) cells that suffer severely from increased temperature and high illumination intensities (NREL and HOLST); (ii) cells that show consistent linear degradation over all times (ISE, IAPP, RisøP); and cells that exhibit improved stability at longer stress times (IMEC and RisøS).

Fig. 6 displays the degradation of all the different solar cells investigated within the cycle experiment as characterized under the accelerated stress condition of full sun illumination and elevated temperatures of up to 85 °C at Risø DTU. From these curves the apparent *TXX* lifetime data were extracted in comparison to the initial power conversion efficiency at the start of the experiment, where *XX* stands for a number between 100 and 0 corresponding to the fraction of initial PCE that is measured at a given time *T*.[14] The PCE plot over stress time usually exhibits two regions: (i) a rapid degradation ("burn-in") occurring exponentially within the first 50–100 hours, and (ii) a slower linear reduction of the PCE between 100 and 600 hours. Notable exceptions are the solar cells from NREL and HOLST, which exhibit a rather rapid degradation up to complete device failure within 200 hours. Furthermore, RisøP and especially the IMEC device showed an improved stability with only gradual

losses in PCE over longer test times. Please note that the high noise level of the NREL cell is due to difficulties in contacting the device by crocodile clamps. Due to this problem noisy *IV*-characteristics occur also in Fig. 22. Nevertheless these contact problems do not constrict the qualitative conclusion drawn for the NREL device.

Table 1 shows the exact times of continued stressing and the relative device performances given in nominal lifetimes *TXX*. The *TXX* values in the brackets correspond to the PCE data from Fig. 6 and correspond to the LBIC measurements, whereas the other values were obtained from *IV*-characterization at TU Ilmenau at the exact times, when the imaging characterization by DLIT, ELI and PLI took place. The discrepancies between the PCE and corresponding *TXX* values obtained at Risø DTU and TU Ilmenau have to be assigned to the time delay upon shipping of the cells and to different illumination sources for solar simulation. This means especially that even the *T*100 values of efficiency were differing due to the same reasons. A notable exception was found only in the case of the ISE cells: complete agreement was found between Risø DTU and TU Ilmenau *IV*-characterization.

In general, a good agreement was found between the cycle degradation experiment and the data obtained from the first experiment without the interruption for imaging characterization (refer to Fig. 8 in ref. 15). Only the IAPP devices did show a different degradation behavior due to the removal of encapsulation for the studies in the cycle experiment. It is evident that from the degradation plots alone no degradation mechanisms can be deduced conclusively. These may be obtained reliably only by detailed destructive elemental analysis over the depth of these devices, which will be the topic of a following publication. However, within this report we demonstrate the possibilities of clarifying the underlying degradation mechanisms with the help of non-destructive imaging and *IV*-characterization alone.

In the following sections, the specific advantages of the several imaging methods with respect to their ability of sensing certain degradation features are discussed. Then the degradation acting on each of the seven different devices is reviewed and discussed based on the most appropriate imaging results. It is necessary to note that all images are given in relative intensity units, since the large variety of different devices studied required individual measurement conditions for each of them. Hence images contain relative, but not absolute quantitative information, which is indeed sufficient for the analysis presented here. Thus all imaging data are quantitatively comparable within a single image; however, this is not possible between different images. Here different signal-to-noise ratios tell much about the absolute signal strength and thus ultimately allow comparisons.

3.1 Specific advantages of imaging techniques and their comparison

In this section we want to briefly discuss which imaging method is most sensitive for detecting specific degradation features, or—in other words—measures the functionality of certain layers or interfaces with best accuracy.

3.1.1 Laser-beam induced current—LBIC. Due to the local nature of the excitation by the laser beam induced current method, relatively small photocurrents are generated that flow through the entire device. As a consequence the serial resistance of the device—mostly imposed from the lower conductive semi-transparent electrode—does not impose any limitation and resistive losses are minimal. Hence smallest variations in the local photovoltaic response can be easily detected. As the photocurrent is generated in the photoactive layer and requires passing through the local active layer–electrode interface, the whole photovoltaic functionality is locally probed by this technique. This in turn enables a clear discrimination between photovoltaically active and inactive regions of the solar cell device at the highest sensitivity.

Proper functioning and not degraded devices therefore yield a very homogeneous response pattern (as seen in Fig. 7a). However, once certain parts of the device suffer from degradation, their LBIC response is lowered or completely fails (as shown in Fig. 7b). Fig. 7 compares a fully operating and a considerably degraded device prepared by vacuum processing by the IAPP group.[24]

However, while the LBIC method identifies proper functioning regions of the solar cell with great accuracy, it is not able to distinguish between the layer or interface that causes the failure at regions, where no current response is given. For example, it is not clear, whether an electrode delaminated from the active layer (interface degradation) or whether the active layer itself is photo-degraded. Furthermore, no local shunting of the device can be detected as these regions will simply appear without photocurrent response as well. In addition, application of the LBIC method always requires a trade off between the

Table 1 Overview of accumulated stress times under accelerated full sun simulation and consecutive imaging characterization as well as corresponding to the degradation defined *TXX* lifetime values. Most of the *TXX* values were changed following shipping of the samples from Risø DTU (values in brackets) to TU Ilmenau

Solar cell type	Time elapsed under accelerated aging in h	*TXX* value for initial imaging	Time elapsed under accelerated aging in h	*TXX* value for second imaging	Time elapsed under accelerated aging in h	*TXX* value for third imaging
IAPP	0	*T*100	42	*T*72 (*T*09)[a]	637	*T*01 (*T*14)
IMEC	0	*T*100	23	*T*30 (*T*54)	618	*T*30 (*T*43)
NREL	0	*T*100	25	*T*50 (*T*36)	217	*T*00 (*T*00)
HOLST	0	*T*100	42	*T*55 (*T*71)	356	*T*00 (*T*00)
ISE	0	*T*100	42	*T*78 (*T*78)	637	*T*38 (*T*38)
RisøP	0	*T*100	42	*T*45 (*T*74)	637	*T*00 (*T*03)
RisøS	0	*T*100	42	*T*44 (*T*62)	637	*T*03 (*T*13)

[a] The large difference in *TXX* for the IAPP samples for second imaging is due to some contacting problems, which were solved at TU Ilmenau later.

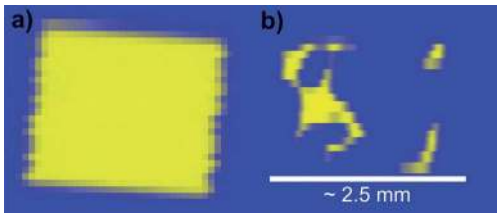

Fig. 7 IAPP vacuum processed device after preparation with full functionality (*T*100) (a), and after considerable degradation (*T*14) (b). Clearly, for the degraded device most of the active area regions remain without current response, revealing the local degradation pattern.

speed of image recording and resolution of the image due to the fact that individual points of the cell have to be scanned subsequently by the laser spot. However, the performance of the Risø DTU LBIC setup is considerably improved over traditional ones, enabling imaging times below one minute.

3.1.2 Dark lock-in thermography—DLIT. Dark lock-in thermography monitors all effects that generate heat within the device upon biasing with a periodically applied external excitation voltage. As a consequence any resistive losses occurring upon current flow can be detected due to the high sensitivity of this method. This fact makes this method the first choice in detecting even small shunts that cause local failure of the solar cell. These are optimally identified by application of a small reverse bias, allowing no current to flow over the diode of the active layer.[25] Under forward bias the larger currents injected and transported through the active layer and the electrodes additionally enable the identification of photovoltaically active regions under reverse operation (driven as an OLED) within the solar cell. Due to the global excitation of the device, series resistance effects become visible, leading to an inhomogeneous heat emission pattern in the direction of current flow through the higher resistive electrode upon current crowding.[22,25,26] Fig. 8a shows a partly degraded device prepared at the IMEC group[27] at its initial characterization (therefore termed *T*100) by DLIT under forward bias. Regions of lower heat dissipation indicate local failures and the rising signal towards the right side displays the effect of series resistance originating from the ITO electrode. The high sensitivity even enables visualization of current transport through the higher resistive semitransparent electrode between the active region of the solar cell and the external contact used for excitation (right side of the device, Fig. 8a). The comparison of DLIT images of a RisøP device[13,28] under forward and reverse bias reveals the presence of many parasitic local shunts, which become clearly visible and distinguishable only under reverse bias (Fig. 8c). Under forward bias and thus larger injection currents the inhomogeneous heating of the current collecting silver comb yields higher intensities (Fig. 8b), making the shunts less visible.

As the DLIT signal originates from thermal emission, the resolution is naturally limited by the wavelength of the IR spectrum and the finite pixel size (typically 15 μm) of the detecting camera. In addition, heat propagation can severely limit achievable resolution and has to be minimized by properly adjusted electrical excitation frequencies.

3.1.3 Electroluminescence imaging—ELI. Electroluminescence imaging directly probes the reverse functionality of solar cells by passing a forward current through the device. The solar cell is operated as an organic light emitting diode (OLED), however, the electroluminescence efficiency is greatly reduced by few orders of magnitude as compared to OLEDs. Hence very sensitive and linearly responding detector arrays are required to detect quantitative signals. By passing the injection current through the electrode–active layer contact and causing radiative recombination within the active layer the functionality of current transport through the active layer and these interfaces is probed simultaneously. Due to the relatively high resolution obtainable by *e.g.* state-of-the-art Si-CCDs, electroluminescence imaging is the method of choice for probing the intactness of the active layer–electrode interface. Due to the global nature of excitation, series resistance effects cause inhomogeneous emission pattern due to the resistivity of the semitransparent electrode.[12,22] Fig. 9a

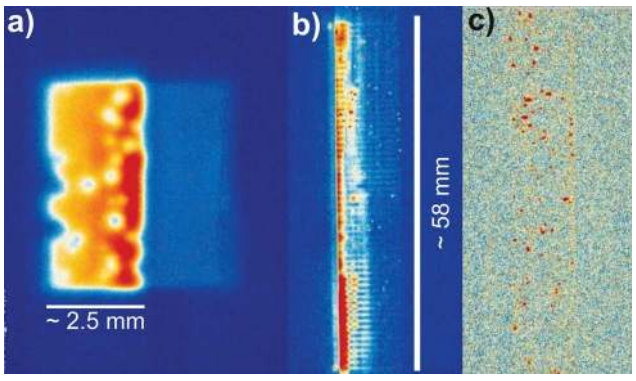

Fig. 8 IMEC processed device at its initial DLIT characterization (*T*100) (a) excited under forward bias. Clearly the functionality of the device is probed up to the detection of even minor series resistance losses occurring within the ITO electrode (right side of the cell). RisøP device at its initial DLIT characterization (*T*100) under forward bias (b) and reverse bias (c). The reverse bias DLIT image clearly shows many local shunts limiting the device performance.

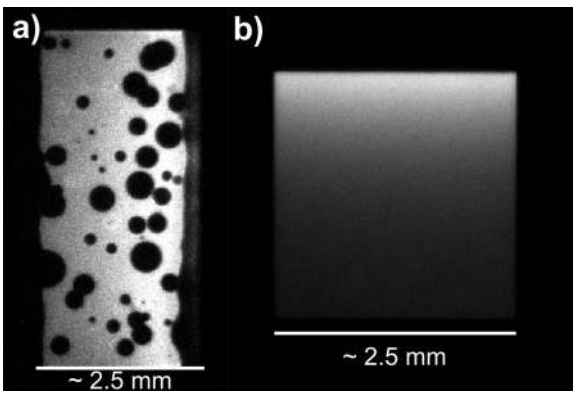

Fig. 9 IMEC processed device at its initial ELI characterization (*T*100) (a) excited under forward bias. Clearly the reverse functionality of the device is probed and regions of contact delamination, typically exhibiting circular structures, can be detected at high accuracy. An IAPP vacuum processed device after preparation with full functionality (*T*100) (b) displays the typical inhomogeneous emission pattern indicating series resistance effects arising from the ITO-electrode.

displays the same IMEC processed solar cell as shown in Fig. 8a. The border between proper functioning device regions and regions of delaminated contacts appears with much higher accuracy than by DLIT (compare Fig. 8a), enabling quantitative measurement of the unspoiled electrode–active layer area.[12] Furthermore, a series resistance limited inhomogeneous emission pattern can be seen, which is even more pronounced for the IAPP (*T*100) device (Fig. 9b). On the one hand, the series resistance caused inhomogeneous emission pattern can be used to characterize the balance between series resistances present in the photoactive layer and the electrode,[22] on the other hand this effect causes difficulties in making the whole device properly visible by ELI. However, this effect can be in part circumvented by properly adjusting the forward bias in combination with the image recording time. One drawback of ELI is the fact that no discrimination can be made between degradation of the photoactive layer and the active layer–electrode interface, a drawback, which can be fortunately overcome by simultaneous recording of photoluminescence images (PLI). However, detailed knowledge of the device structure and its materials is required to understand which electrode interface fails within the device.

3.1.4 Photoluminescence imaging—PLI. Due to the fact that photoactive materials do exhibit some minor photoluminescence response, photoluminescence imaging can be applied to monitor the integrity of the organic semiconductors. However, as the photoluminescence signal of photoactive bulk heterojunctions is generally reduced by orders of magnitude as compared to *e.g.* pristine conjugated polymers, very sensitive and linearly responding detector arrays are required in order to probe the photoluminescence signal quantitatively.[12] Since the excitation light has to be blocked from entering the detector, cut-off filters are applied. However, even greatly reduced reflections may enter the system, as cut-off filters still enable passing of small amounts of light that are comparable to the photoluminescence signal. Hence a combined response from photoluminescence and reflection of excitation light is detected, an apparent drawback that can be exploited in some cases for quality control issues.[29] Fig. 10 displays three ISE processed solar cells[30] on a single substrate, clearly allowing high resolution discrimination between intact active layer regions and those that suffer from oxygen and water ingress through the edges of the sealing. Thus PLI is a very rapid characterization method yielding overview information on (photo-) degradation of organic semiconductors, but contains only minor information (*e.g.* by reduced reflection) about the integrity of the electrodes, and the respective electrode–active layer interface.

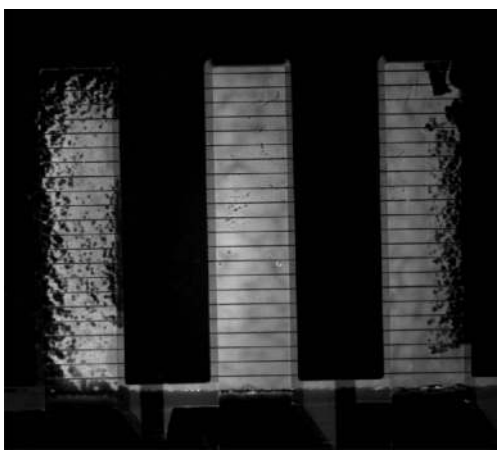

Fig. 10 ISE processed, glass-to-glass sealed, polymer solar cell at its initial photoluminescence/reflection imaging characterization (*T*100). The active layer degradation upon oxygen and water vapor ingress from the edges of the sealing is clearly visible.

3.1.5 Combination of all imaging techniques for conclusive degradation analysis. In this section an example is given, which demonstrates the benefit of applying a combination of imaging methods, for the determination of the degradation mechanisms responsible for device failure. Fig. 11 displays all images obtained by the above discussed methods on an NREL device[10] at a state of intermediate degradation (*T*50). After 25 hours under full sun and elevated temperature stress conditions, the unsealed device exhibits a manifold of degradation features. The LBIC image displays only a partly and spatially distributed photovoltaically active device (Fig. 11a). These features of device operation are exactly reproduced within the ELI characterization at a higher spatial resolution (Fig. 11b), also showing the strongly reduced operation under forward bias (reverse mode as an OLED). As a point for orientation and comparison in all images an "ET-face" feature can be spotted in the lower center section of the images (marked by a red circle). Darker parts in the LBIC and ELI images thus indicate regions of degraded active layer–electrode interface—presumably occurring at the PEDOT:PSS–silver interface.[10] The PLI characterization (Fig. 11c) reveals the identical features at lower contrast, allowing however a better discrimination between active layer degradation (fully dark regions) and contact delamination (grey regions) by step-wise differences in their respective brightness and upon comparison with the ELI image. Finally, DLIT forward and reverse (Fig. 11d and e) bias recordings point out that the device suffers from severe local shunting, whereas the photovoltaically active regions are barely visible. Interestingly, the ELI image reproduces two of these local shunts by highly increased local signals. Either this has to be explained by locally corresponding highly increased electroluminescence signal, or the Si-CCD is capable of capturing part of the heat radiation within its near-infrared sensitive spectrum. However, two shunts visible by the DLIT method remain completely dark in the ELI image, expressing the necessity for the highly sensitive DLIT measurement. In conclusion, it is obvious that one method alone cannot satisfyingly record all features at sufficient resolution. Hence our approach of combining these complementary imaging techniques is clearly justified: LBIC shows the local photovoltaic operation, ELI monitors the injection across the degraded electrode–active layer interface, PLI specifically reveals the degraded active layer regions and DLIT yields the information about locally occurring shunts.

3.2 Device specific degradation patterns

As indicated in the last section, a suitable combination of imaging methods enables the individual analysis of the degradation mechanisms acting on each of the different devices produced and characterized within this study. By consideration

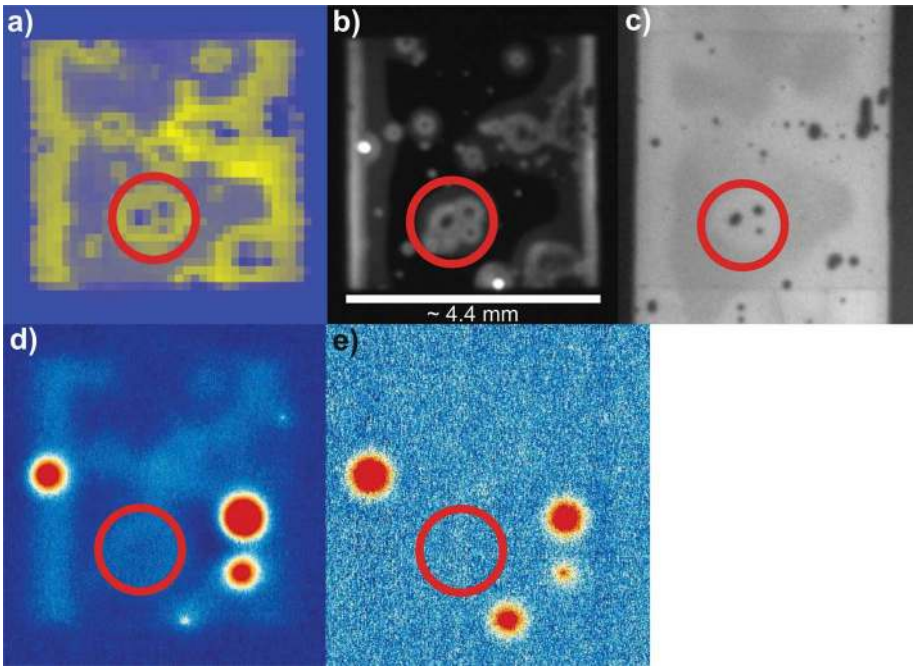

Fig. 11 Combination of information obtained by LBIC (a), ELI (b), PLI (c) and DLIT forward (d) and reverse (e) imaging on a solar cell prepared by the NREL group after degradation (*T*50). LBIC and ELI clearly show the photovoltaically active regions in normal and reverse operation, respectively. PLI allows better discrimination between photoactive layer degradation through pinholes (black circular regions) and electrode delamination (darker grey regions). Finally, DLIT forward and reverse operations point out 4–5 local shunts, differently active in both bias directions.

of the device architecture, materials incorporated and the corresponding *IV*-characteristics, the maximum information possible by imaging analysis was extracted to determine the degradation mechanisms for all solar cells provided by the manufacturing groups. Within this section only the seven devices from the cycle experiment are considered. Other devices, stressed without interruption and characterized for destructive analysis, were imaged as well. However, this is beyond the scope of this article and will be discussed in a following report.

3.2.1 ZnPc:C60 vacuum processed device on glass—IAPP. The IAPP device contains a vacuum processed ZnPc:C60 bulk heterojunction sandwiched between suitable organic hole and electron transport layers that connect to the ITO hole-extracting and aluminium electron-extracting electrodes, respectively.[24] Due to the superior glass–glass encapsulation and high temperature stability of the evaporated materials, these devices did not show any degradation over a thousand hours. Hence the encapsulation was removed from some devices to enable and investigate their degradation. The resulting degradation under full sun illumination could be monitored successfully by ELI characterization (as shown in Fig. 12): typical lower work function electrode delamination features caused by water and oxygen ingress through edges of the cell and through pinholes in the aluminium electrode led to shrinkage of the effective active area of the device (Fig. 12b).[12] After more than 600 hours of continued stress the device failed almost completely, leaving only a microscopic device area with intact aluminium contact (Fig. 12c). All electroluminescence images were obtained under the same excitation conditions of 1.5 Volts forward bias. LBIC yielded qualitatively identical images at lower resolution, confirming the degradation pattern. Fig. 13 shows the *IV*-characteristics at corresponding times when the ELI measurements were done. A fairly good correlation between short circuit photocurrents and effective active device area is found, supporting the postulated degradation mechanism. A sketch of the device structure and the degradation model mentioned above is depicted in Fig. 14.

3.2.2 P3HT:PCBM solution processed device on glass—IMEC. The solution processed IMEC device based on a P3HT:PCBM active layer exhibited very particular degradation features. The unencapsulated device was fashioned in an inverted structure, extracting the electrons through a thin ZnO interlayer over the ITO-electrode. The vacuum processed hole extracting electrode consisted of a 10 nm MoO_3 interlayer, followed by a silver and an aluminium layer.[27] The degradation mechanism can only be understood by a combination of all imaging characterizations.

The initially characterized device exhibited already considerable electrode delamination features clearly visible by the black holes over the entire device area (see Fig. 15a) upon imaging by ELI. Furthermore there was a delamination from the long side edges of the back electrode visible. We interpret this delamination to be due to the oxidation of the silver (Ag_xO) at the MoO_3 interface. After 25 hours of full sun simulation and degradation to *T*30 the ELI image reveals a reversal of behavior (Fig. 15b): the previously observed delaminated edges and black holes yield brighter regions, except for smaller center holes within. The overall emission intensity became lower, especially for the central device regions—previously assigned to non-delaminated and thus non-oxidized silver.

Interestingly these regions exhibit larger heat dissipation as evident from the DLIT image in Fig. 16b. Hence the current

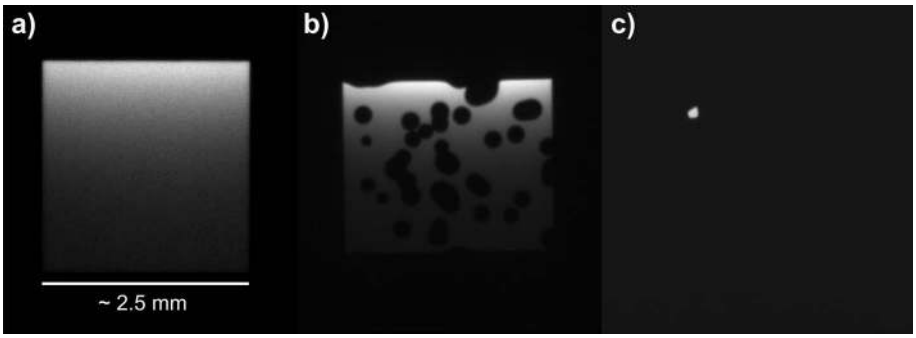

Fig. 12 IAPP solar cell from the cycle experiment without encapsulation: initially at *T*100 (a), after 42 hours at *T*72 (b) and after total 637 hours under full sun simulation at *T*01 (c). All images were recorded under 1.5 Volts forward bias.

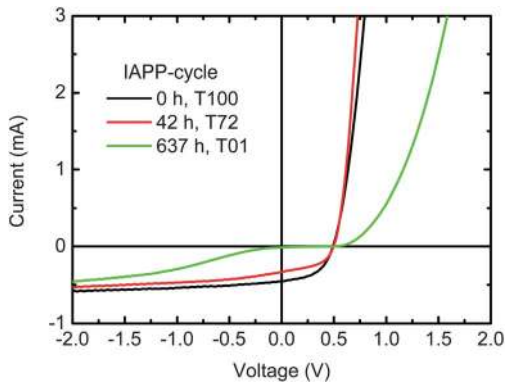

Fig. 13 *IV*-characteristics of the IAPP cycle cell with progressing degradation at times of ELI characterization. After more than 600 hours continued illumination, the device—exhibiting a clear blocking contact feature—almost completely failed. The active cell area of this device is 0.0635 cm^2.

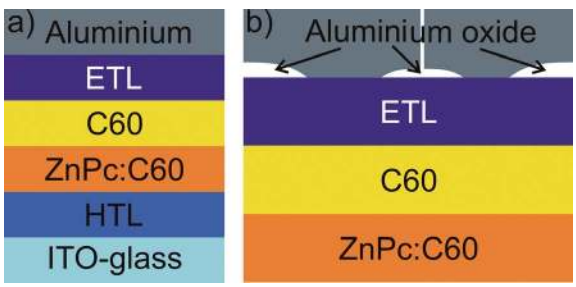

Fig. 14 Device structure (a) and predominant degradation mechanism (b) of the IAPP processed solar cells as determined by imaging characterization. Upon free exposure to air within the degradation setup, the aluminium electrode is the first to be oxidized—either by water and oxygen ingress from the sides or through pinholes. As a result, the effective active area is reduced and finally a fully blocking Al_2O_3 interlayer is formed.

densities flowing over this region must be larger, which is in agreement with a smaller series resistance as compared to the other regions that exhibit an increased series resistance due to the presence of Ag_xO. Even though the current densities within these regions must be larger, the electroluminescence is greatly reduced (Fig. 15b). This behavior can be understood, if the holes are no longer injected into the HOMO of the P3HT, but into the LUMO of the PCBM. In other words, electrons get directly extracted from the top electrode. Thus, under forward bias the solar cell has locally turned into a single carrier device for electrons. The preferred electron extraction over hole injection is a clear sign for a decrease in the work function of this compound electrode.

Furthermore, the LBIC measurements (Fig. 18) clearly show that the photovoltaic operation is not disturbed within these regions and remains active over the entire device area even after 618 h of full sun simulation, in good agreement with the *IV*-characteristics (Fig. 19). This behavior can be well understood as according to the PLI the photoactive layer remains—except for some smaller dark spots at the pinholes—almost fully intact (see Fig. 17). In fact at the intermediate degradation stage (Fig. 18b) the photocurrents extracted here are larger than in the regions where the electroluminescence is higher. In other words, the hole extraction at this electrode remains efficient, regardless of a work function decrease. In conclusion, the increased injection barrier for holes and their barrier-free extraction are in line with a local decrease of the electrode's work function.

As a reduction of the MoO_3 appears rather improbable, another material must control the work function at the electrode–active layer interface. Silver is known for its tendency to migrate and a 10 nm thick and partly amorphous MoO_3-interlayer can neither be assumed to be defect free nor to be impermeable for silver atoms. Furthermore the far higher (at least three orders of magnitude) free electron density of silver can decrease the work function already at modest loadings. Hence silver penetration into the thin MoO_3 interlayer can explain the change in the injection and extraction behavior.

This proposed decrease in work function of the back electrode affects the solar cell by a considerably decreased photocurrent and an only slightly decreased open circuit voltage (Fig. 19). Thus the observed decrease in photocurrent can be assigned to a lower work function difference between electron and hole extracting electrodes, acting as the driving force for charge extraction, and possibly oxygen doping of the photoactive layer.[9] Furthermore the change in the open circuit voltage for the degraded device confirms a change of the injection/extraction properties and thus changes at the initially pristine MoO_3–active layer interface.

At later stages of degradation (compare with Fig. 15c), only small fringes around the positions of the pinholes and near the

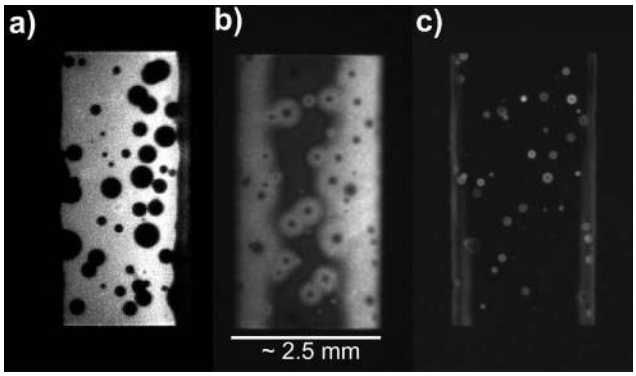

Fig. 15 ELI characterization of the IMEC solar cell from the cycle experiment without encapsulation: initially at nominally *T*100 (a), after 23 hours at *T*30 (b) and after total 618 hours under full sun simulation at *T*30 (c). Reversal of the spatial electroluminescence intensity occurring with time is observed and can be understood by the formation of a blocking layer for hole injection but unhindered extraction within the central device regions. All images were recorded under 1.5 Volts forward bias.

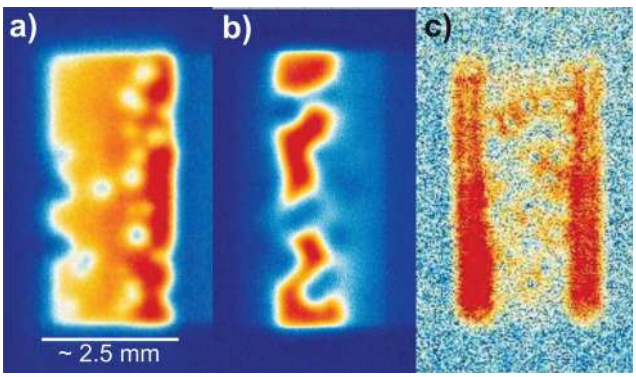

Fig. 16 DLIT characterization of the IMEC solar cell from the cycle experiment without encapsulation: initially at nominally *T*100 (a), after 23 hours at *T*30 (b) and after total 618 hours under full sun simulation at *T*30 (c). All DLIT images exhibit the same features as observed with ELI (Fig. 15), however, after 23 hours stressing the center parts appear with relatively higher intensity due to resistive heating upon more efficient current injection. The first image was recorded at 1 Volt, the other two at 1.5 Volts, forward bias.

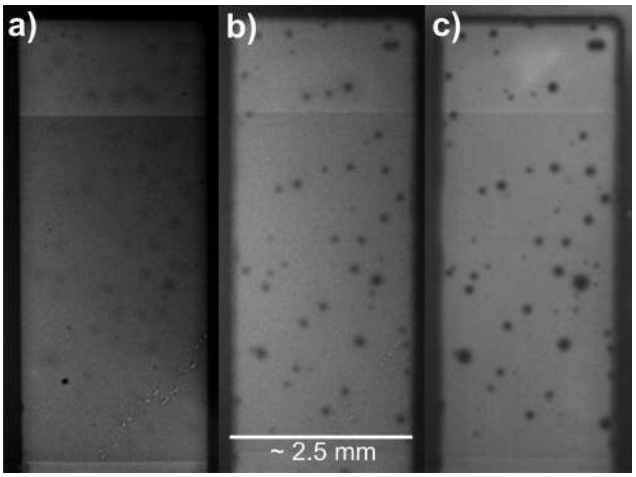

Fig. 17 PLI characterization of the IMEC solar cell from the cycle experiment without encapsulation: initially at nominally *T*100 (a), after 23 hours at *T*30 (b) and after total 618 hours under full sun simulation at *T*30 (c). The dark points distributed over the electrode region correspond to points of pinhole ingress of water and oxygen. Not only the reflectivity of the electrode is changed, but also active layer photo-oxidation leads to a reduced PLI signal.[12,32]

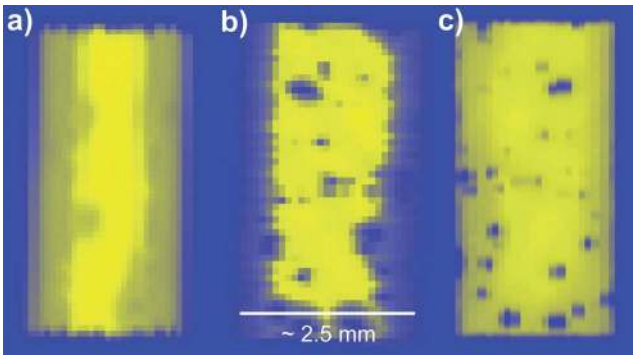

Fig. 18 LBIC characterization of the IMEC solar cell from the cycle experiment without encapsulation: initially at nominally *T*100 (a), after 23 hours at *T*30 (b) and after total 618 hours under full sun simulation at *T*30 (c). The LBIC images reveal photovoltaic operation and charge carrier extraction over the whole device, except for the regions degraded by pinhole ingress—in contrast to ELI and DLIT.

outer edge of the device can be observed in electroluminescence. Hence injection of holes remains possible only near the edges of pinholes and the rim of the electrode, pointing to an edge controlled electric field enhancement. All other areas do not provide sufficient electric fields, or hole injection is prohibited by the decreased work function. In fact some minor injection of charge carriers can be still observed besides the pinhole positions in the lock-in thermography images (Fig. 16c), which has to be related to electron extraction as pointed out before. In contrast, the LBIC signal, operating with much smaller total currents, remains vital throughout the device area except for the locations of pinholes and near the edges of the device (Fig. 18c). The low (DLIT) or no (ELI) signals for charge injection and the efficient charge extraction (LBIC) indicate the formation of a fully covering blocking contact, as directly visible from the *IV*-characteristics (Fig. 19). The point of inflection is located at the open circuit voltage, putting up a symmetric blocking behavior for extraction and injection.

All of the above device characteristics and imaging results are in good agreement with the following model proposed for the electrode and thus the dominant device degradation channel (compare with Fig. 20): (i) initially, silver penetration into the MoO_3 interlayer and silver oxidation are taking place in competition; (ii) at locations of silver penetration the acting work function in direct vicinity to the photoactive layer becomes reduced; (iii) at later stages a blocking contact feature occurs. Oxygen penetration into the device may result in increasing barriers for charge injection and extraction by formation of silver-oxide or by dedoping effects at the ZnO interlayer.[31]

Since this counter diode acts only in the first quadrant as long as the blocking behaviour is small enough, it does not lower the device efficiency in photovoltaic operation (fourth quadrant)

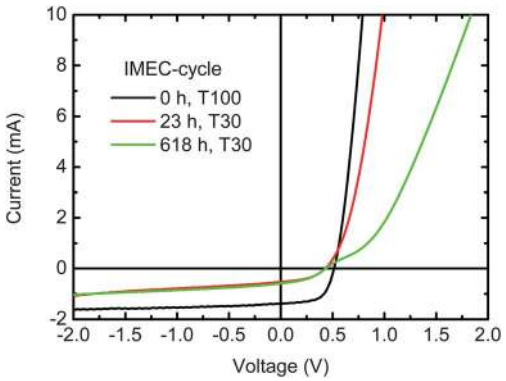

Fig. 19 *IV*-characteristics of the IMEC cycle cell with progressing degradation at times of ELI/DLIT characterization. Clearly a drastic change in the device functionality is observed after only 23 hours under accelerated full sun simulation, leading to a slight reduction in the open circuit voltage, but more severe one in photocurrent. Within more than 600 hours continued illumination, the device develops a blocking contact feature, which can either be assigned to the formation of a silver-oxide or an oxygen dedoped ZnO interlayer. The active cell area of this device is 0.134 cm^2.

even upon stressing times of up to 618 hours. Only at regions with increased electric field strength, occurring near edges such as the borders of pinholes, and pristine MoO_3 interlayer, charge

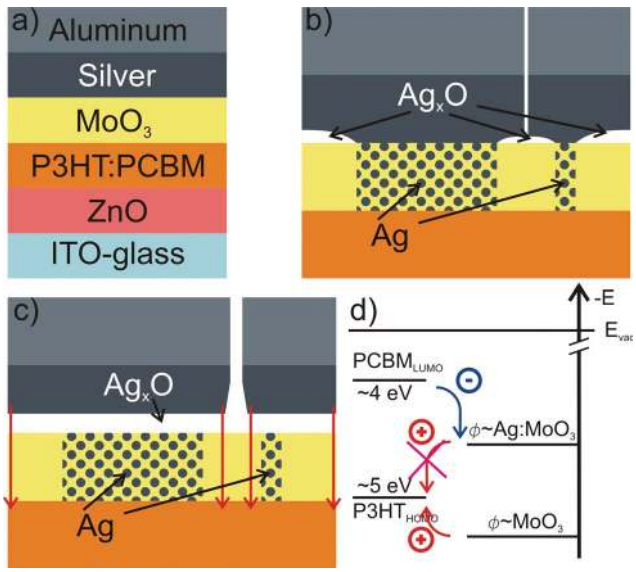

Fig. 20 Device structure (a) and probable degradation mechanism (b and c) of the IMEC processed solar cells as determined by imaging characterization. The silver–MoO_3 interface appears frail to interpenetration of Ag into the MoO_3, which exhibits a lower resulting work function than the pristine MoO_3. Hence, the open circuit voltage of the solar cell gets reduced and hole injection into the HOMO of P3HT is hindered. Silver-oxide and/or ZnO-dedoped blocking layers are formed either by water and oxygen ingress from the sides or through pinholes. This silver-oxide layer appears to locally suppress the interpenetration of silver. After formation of a completely covering silver-oxide layer, charge injection is only possible at places of edge-increased electric field strength (red arrows in c), however, charge extraction remains less hindered. An energy scheme (d) displays the possible changes at this interface.

injection remains possible (see red arrows in Fig. 20c and fine scaled features in Fig. 15c). Since reverse DLIT imaging did not reveal any shunting features, continued silver migration must be hindered by the silver-oxide layer on top of or by the MoO_3 interlayer itself.

Although the model proposed above, especially the penetration of silver into the MoO_3, can be an explanation to the observed behavior, it might not be the only one. However, a change in the work function of the hole extracting electrode appears to be the best explanation to the observed imaging features. Clear evidence about the processes taking place on the atomic scale needs to be elaborated *via* by far more sensitive probing techniques.

3.2.3 P3HT:PCBM solution processed device on glass—NREL. The unencapsulated solution processed NREL device[10] based on a P3HT:PCBM active layer exhibited nearly the identical architecture as the IMEC device. The only difference in the device structure is the use of a PEDOT:PSS interlayer instead of the MoO_3. A difference inducing drastic consequences: after a total 217 hours under full sun illumination the solar cell completely failed. The reason for that failure was found solely by DLIT imaging: massive shunting occurred over large regions of the device, leaving no room for photovoltaic operation (compare with Fig. 21). This shunting occurred predominantly at the places where injection remained possible after silver oxidation—around pinholes and at the edges of the metal electrode. Hence we can conclude that electro-migration of silver led to penetration of the 40 nm thin PEDOT:PSS interlayer, which is by far less dense than a MoO_3 interlayer. Fig. 21 summarizes the temporal development of the degradation which is otherwise similar to IMEC devices. The corresponding *IV*-characteristics are given in Fig. 22 for comparison. The final shunting is clearly visible from the *IV*-curve after 217 hours stressing.

As shown above in Fig. 11 the complex degradation behavior possibly due to silver oxidation or ZnO-dedoping appears similar to the IMEC device degradation, except for the occurrence of the shunts upon electro-migration of the silver. Fig. 23 summarizes the predominant degradation mechanisms.

3.2.4 P3HT:PCBM solution processed ITO-free device on glass—HOLST. The solution processed HOLST device based on a P3HT:PCBM active layer was prepared on a silver grid/highly conductive PEDOT:PSS hybrid front electrode as a replacement for ITO. The device was encapsulated between the glass substrate and a stainless steel plate. The electron extracting back electrode was realized by 1 nm LiF topped by 100 nm aluminium.[33]

The degradation mechanism of the HOLST cell could be best captured with DLIT and LBIC characterization as shown in Fig. 24. Assuming a gradually increasing interface oxidation of the LiF/aluminium back electrode provides the best possible explanation for the characteristic degradation pattern observed. The degradation was only observed for the device kept under accelerated full sun simulation, similar devices kept in the dark or under low intensity fluorescent lamp were only slightly degrading over 1800 hours of operation.[15] A key for understanding is therefore the increased photocurrents and the higher temperature under full sun simulation. Both factors result possibly in water release from the PEDOT:PSS layer taking place at regions

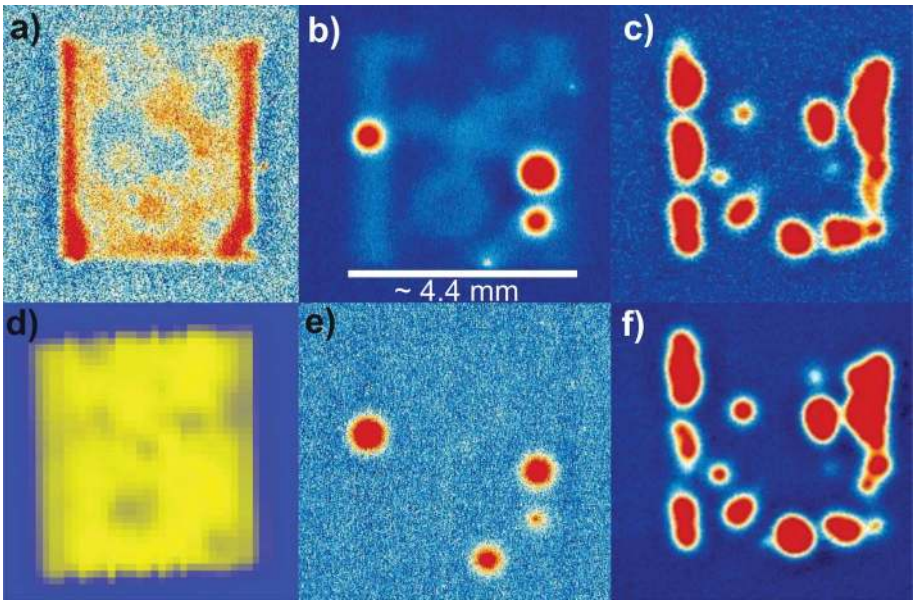

Fig. 21 DLIT characterization of the NREL solar cell from the cycle experiment without encapsulation: initially at nominal *T*100 (a), after 25 hours at *T*50 (b and e) and after total 217 hours under full sun simulation at *T*00 (c and f). The upper row shows the images obtained by 1.5 Volts forward bias excitation, the lower row shows the images obtained at −1.5 Volts reverse excitation and the initial operation (*T*100, Risø DTU) detected by LBIC (d). Clearly the features present at *T*50 and *T*00 are dominated by parasitic shunting.

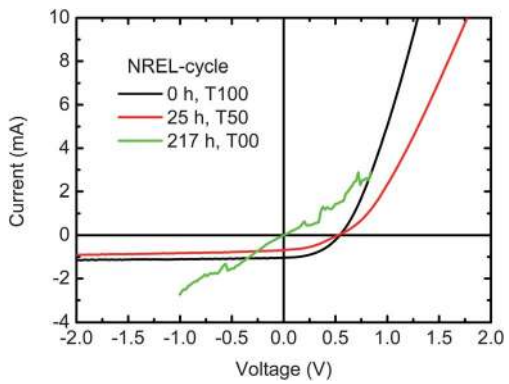

Fig. 22 *IV*-characteristics of the NREL cycle device at initial (*T*100), after 25 hours (*T*50) and after 217 hours (*T*00) under full sun illumination. After 25 hours stressing, the device exhibits initial features of blocking layer formation. At its final stage the device suffered from massive shunting, visible in the *T*00 *IV*-curve that crossed the origin of the current–voltage plot. Contacting problems led to the peculiar noisy *IV*-recording. The active cell area of this device is 0.11 cm^2.

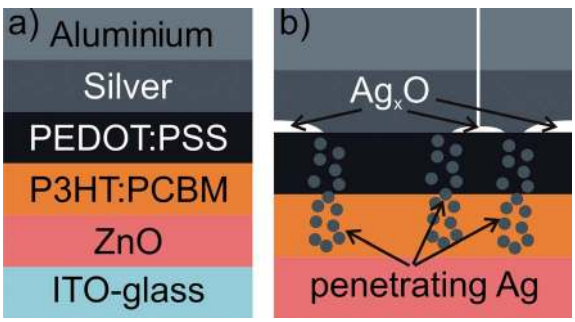

Fig. 23 Device structure (a) and degradation mechanism (b) of the NREL processed solar cells as determined by imaging characterization. Besides oxidation of the silver–PEDOT:PSS interface, silver is able to penetrate—possibly driven by electro-migration—through the thin PEDOT:PSS and the photoactive layer, resulting in shunts that lead to complete device failure.

with increasing current density. As a result, the aluminium electrode correlated with that current transport oxidizes first.[13] This can explain the proper device operation after intermediate degradation in the center of the grids, as there the aluminium electrode was more intact than half way to the grid electrode. However, due to a cooling effect of the silver grid and some possible electric field enhancement near the silver grid, charge carriers could reasonably be easily extracted at the intermediate stage of degradation in direct spatial proximity to the grid structure (*T*55, Fig. 24b and e). The formation of a blocking contact could already be confirmed by the *IV*-characterization for the intermediate state of degradation (compare with Fig. 25). This blocking resulted in the increased electric field dependence for photocurrent extraction. At the final stage of degradation after 356 hours, no photovoltaic response could be detected anymore and the complete aluminium electrode constituted a strong blocking contact. Therefore no response was detectable with LBIC anymore, only DLIT yielded a very weak signal corresponding to very small currents driven through the blocking contact near the silver grid structure exploiting the locally acting electric field.

Fig. 26 summarizes the degradation mechanism detected for the HOLST device: (a) shows the schematic device structure, whereas (b) displays the complex situation at the intermediate degradation stage for a region extending from the silver grid to the center within the honeycomb structure: water release from PEDOT:PSS and thus aluminium interface oxidation occurs first

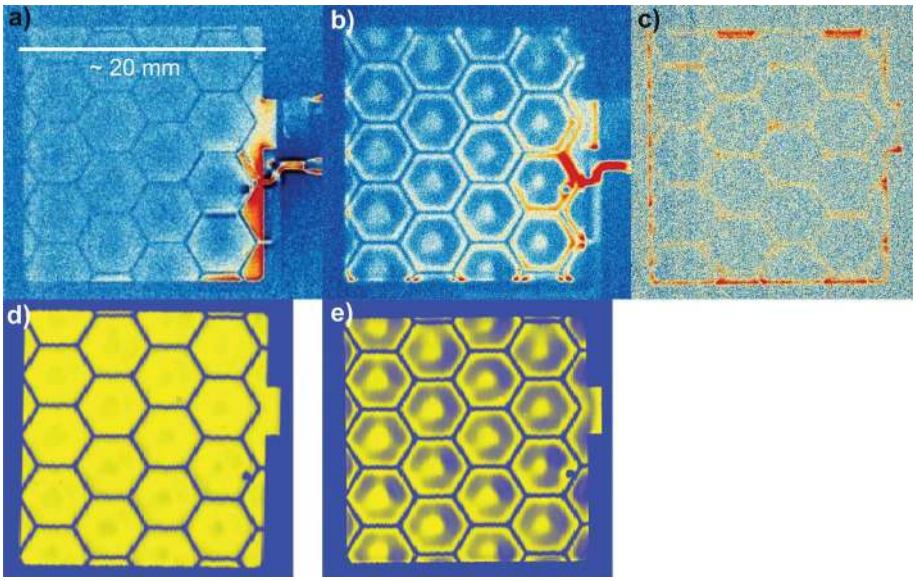

Fig. 24 DLIT (upper row) and LBIC (lower row) characterization of the HOLST solar cell from the cycle experiment: initially at nominal *T*100 (a and d), after 42 hours at *T*55 (b and e) and after total 356 hours under full sun simulation at *T*00 (c). DLIT images were obtained under +2 Volts (a and b) and + 3 Volts (c). As the fully degraded device did not exhibit any photovoltaic response any longer, no LBIC image could be obtained. Starting from a homogeneous operation at *T*100, the second characterization revealed less photovoltaically active regions at about half the distance between the current extracting silver grid electrode and the center of each grid (see text for details).

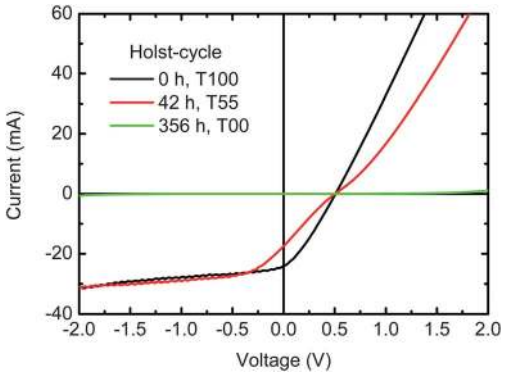

Fig. 25 *IV*-characteristics of the HOLST cycle device at initial (*T*100), after 42 hours (*T*55) and after total 356 hours (*T*00) under full sun illumination. After 42 hours stressing, the device exhibits initial features of blocking layer formation resulting in the reduced fill factor by electric field limited current extraction. At its final stage the device suffered from a fully blocking aluminium electrode interface. The active cell area of this device is 3.78 cm^2.

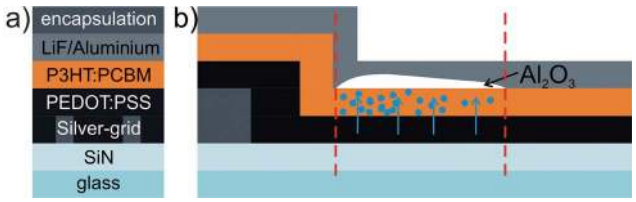

Fig. 26 Device structure (a) and degradation mechanism (b) of the HOLST processed solar cells as determined by imaging characterization. Owing to the elevated temperatures and additional heating of the device due to current collection within the PEDOT:PSS, water is released from the highly conductive PEDOT:PSS layer, resulting in an oxidation of the aluminium electrode first within these regions. At the final stage the complete aluminium electrode is covered by a blocking oxide layer (not shown here), preventing any further device operation.

predominantly with increasing current collection within PEDOT:PSS towards the silver grid due to heating. Within the vicinity of the silver grid electrode oxidation either occurs later due to some cooling effect of the same, or edge effect electric field enhancement facilitates charge injection and extraction at considerable efficiency. At regions far away from the silver grid current collection within PEDOT:PSS results in smaller current densities and the oxidation of the aluminium is delayed, enabling relatively good operation in the center of the honeycomb structure. Finally, the whole aluminium–active layer interface forms a blocking junction due to the oxidation, preventing any photocurrent to be extracted (compare with Fig. 25). A possible oxidation of the silver-grid electrode's interface to PEDOT:PSS is not considered here but is possible as well. However, the dominating degradation mechanism is believed to be related to the oxidation of the aluminium interface, due to its stronger oxidation tendency.

3.2.5 P3HT:PCBM solution processed ITO-free device on glass—ISE. The encapsulated solution processed ISE device based on a P3HT:PCBM active layer exhibited an inverted architecture with a hole extracting top electrode consisting of a highly conductive PEDOT:PSS and a gold grid. The bottom, electron extracting, electrode consisted of a 5 nm Cr/100 nm Al/5 nm Cr layer stack.[30] Note that the gold fingers were contacted from both sides of the solar cell, allowing even current distribution within the global gold electrode. The degradation mechanism is not directly obvious: the LBIC images show decreasing photovoltaic response over time (compare with Fig. 27a–c), which is initially found in between the shading gold stripes and finally predominantly confined near the thin gold grid stripes.

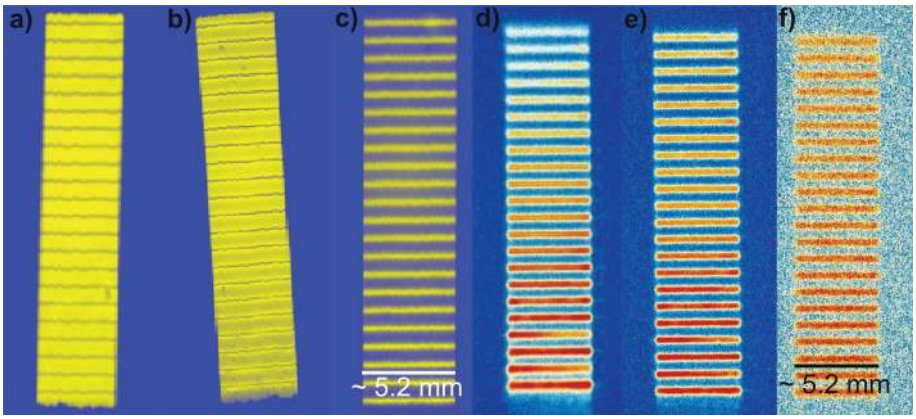

Fig. 27 LBIC (left) and DLIT (right) characterization of the ISE solar cell from the cycle experiment: initially at nominally *T*100 (a and d), after 42 hours at *T*78 (b and e) and after total 637 hours under full sun simulation at *T*38 (c and f). All DLIT images were obtained under +1.5 Volts. LBIC reveals loss in overall photovoltaic response, whereas DLIT reveals an increase in series resistance perpendicular to the cell plane. This increase in series resistance can be assigned to the formation of an oxide layer at the lower work function electrode or increase of the series resistance of the current collection PEDOT:PSS layer (see text for details).

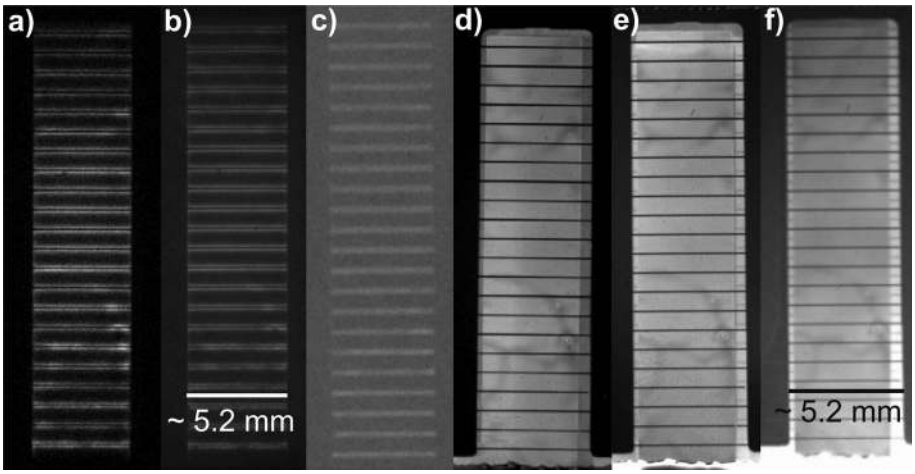

Fig. 28 ELI (left) and PLI (right) characterization of the ISE solar cell from the cycle experiment: initially at nominally *T*100 (a and d), after 42 hours at *T*78 (b and e) and after total 637 hours under full sun simulation at *T*38 (c and f). All ELI images were obtained under +1.5 Volts.

DLIT imaging reveals a difference between the sheet resistances of the two electrodes, leading to a current crowding near the external contact of the lower conductive electrode (compare with Fig. 27d–f).[22,26,34] In this case the aluminium electrode appeared to be the less conductive one.

This feature could be exploited in order to understand the underlying degradation mechanism: with progressing degradation the current density is getting more evenly distributed over the gold stripes. In view of the current crowding this can have two reasons: (i) the sheet resistance of aluminium is increasing and thus balancing the one of gold, or (ii) an evenly distributed series resistance is blocking the current extraction. The second case appears more realistic and can be explained by the same mechanism as found for the HOLST solar cell: heating of the highly conductive PEDOT:PSS layer under thermal and current stress may result in some water release that homogeneously corrodes the electron extracting low work function electrode.

The *IV*-characteristics of the cycle cell plotted over degradation time given in Fig. 29 display an electric field dependent photocurrent extraction—in good agreement with the LBIC

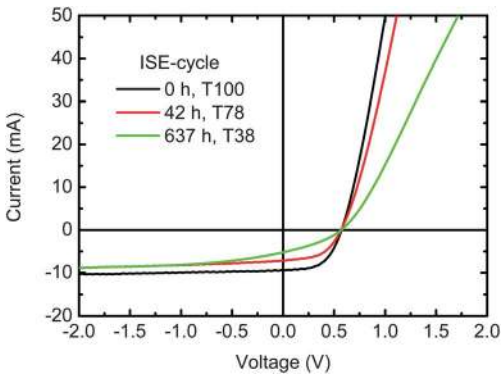

Fig. 29 *IV*-characteristics of the ISE cycle device at initial (*T*100), after 42 hours (*T*78) and after total 637 hours (*T*38) under full sun illumination. After 42 hours stressing, the device only loses part of the photocurrent and exhibits a slightly increased series resistance. After 637 hours of stressing the *IV*-curve exhibits a further increased series resistance and the reduced fill factor appears to be controlled by electric field limited current extraction. The active cell area of this device is 1.1 cm^2.

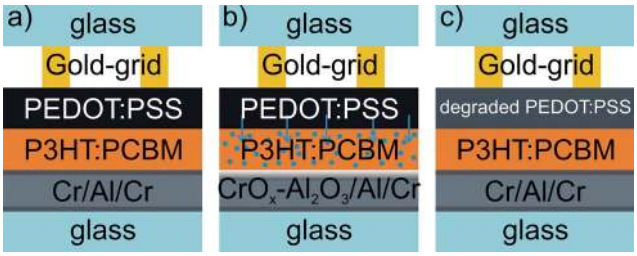

Fig. 30 Device structure (a) and two possible degradation mechanisms (b and c) of the ISE processed solar cells as determined by imaging characterization. (b) Owing to the elevated temperatures and pronounced heating of the device at the gold grid, water is released from the highly conductive PEDOT:PSS layer, resulting in a rather homogeneous oxidation of the aluminium electrode. The oxidation of the aluminium electrode is delayed as compared to other devices by an ultra-thin chromium protection layer at the active layer–electron extracting electrode interface. (c) UV-light causes photo-degradation of the PEDOT:PSS layer, resulting in a decreased conductivity and thus an overall higher sheet resistance and less efficient hole extraction at the anode.

features—for the most degraded device. Interestingly, no blocking layer formation is detected. Only the increase of a series resistance and the lowered fill factor point to the fact that the electron extracting electrode may slowly corrode. Apparently the interfacial chromium layer slows down this reaction considerably. However, the oxidation of both, chromium and aluminium seems feasible especially under elevated temperatures. This electrode corrosion and/or possible degradation of the PEDOT:PSS layer under the present UV-radiation[35] may cause the series resistance increase observed within the *IV*-characteristics (Fig. 29).

Due to the low conductivity of the PEDOT:PSS layer, the ELI characterization results—similar to the case of DLIT—in a current crowding around the gold contact fingers (compare with Fig. 27d–f and Fig. 28a–c). The PLI characterization shows basically intact photoactive layers, so that ingress and oxidation from the sealing edges can be ruled out as a factor for degradation (compare with Fig. 10).

Fig. 30 displays two possible degradation mechanisms of the ISE device: (i) water release from the highly conductive PEDOT:PSS layer may result in the formation of a chromium–aluminium-oxide layer (compare to Fig. 30b); (ii) PEDOT:PSS degradation by photo-oxidation due to UV-light[35] causes further conductivity losses resulting in an overall sheet resistance increase and less efficient hole collection (compare to Fig. 30c).

The charm of this device configuration is the prevention of a blocking contact at the electron extracting electrode, which must be caused by the chromium layer resulting in a considerably slowed down degradation and thus increased lifetime.

3.2.6 P3HT:PCBM solution processed device on PET—RisøP. The flexible encapsulated solution processed RisøP device based on a P3HT:PCBM active layer exhibited an inverted architecture with a hole extracting back electrode consisting of a highly conductive PEDOT:PSS and a silver grid. In contrast to the ISE cell both the PEDOT:PSS as well as the silver grid were printed and exhibited a much larger layer thickness. The semi-transparent, electron extracting, front electrode consisted of a 20 nm ZnO/90 nm ITO layer stack.[13,28] In this case the silver grid lines were contacted only from one side of the solar cell, leading to current crowding near the side-contact due to the limited conductivity and respective finite sheet resistivity. Hence DLIT yielded less homogeneous images of the solar cells, with increasing heat emission near the outer contact of the silver grid lines (compare with Fig. 31). Under reverse bias excitation DLIT reveals many shunting features distributed over the whole cell. For longer aging times after 637 hours of accelerated full sun simulation, the number of shunts increased near the end of the silver fingers pointing out electro-migration of silver at the electric field enhancement due to sharp edges of the electrode. A weaker photovoltaic operation can be deferred from the reduced signal-to-noise ratio in the forward DLIT image as well as by LBIC (not shown here). Remaining indications are extracted from the *IV*-characteristics (Fig. 32): at *T*45 some features of blocking contact appear. This blocking contact feature is either caused by interfacial oxidation of the silver electrode on top of

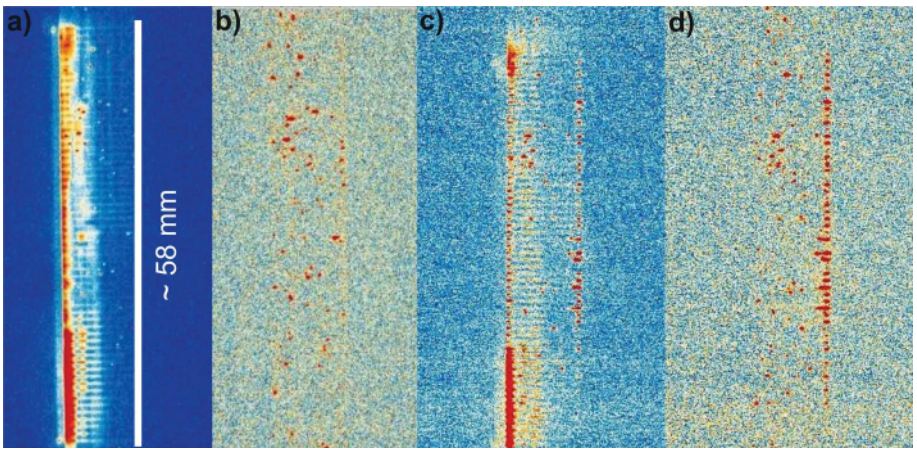

Fig. 31 DLIT characterization of the RisøP solar cell from the cycle experiment: initially at nominal *T*100 (a and b), and after total 637 hours under full sun simulation at *T*00 (c and d). Forward excitation was done at +1.5 Volts (a and c), reverse excitation at −1.5 Volts (b and d). Under reverse excitation DLIT reveals an increase in shunting between the initial and the final characterization. As the new shunting features occur predominantly at the outermost edge of the silver grid lines (right side), electro-migration under edge enhanced electric fields appears to cause the additional shunts.

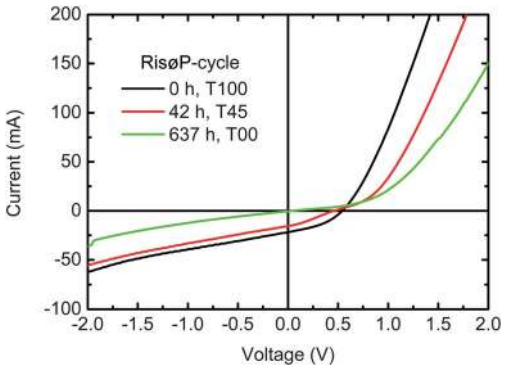

Fig. 32 *IV*-characteristics of the RisøP cycle device at initial (*T*100), after 42 hours (*T*45) and after total 637 hours (*T*00) under full sun illumination. After 42 hours stressing, the device loses part of the photocurrent, exhibits a slightly increased series resistance and reveals a blocking contact respectively counter diode feature. After 637 hours of stressing the *IV*-curve exhibits a further increased series resistance and basically no photovoltaic operation anymore. The influence of shunts on the *IV*-characteristics is evident from the increasing current towards negative voltages. The active cell area of this device is 4.9 cm^2.

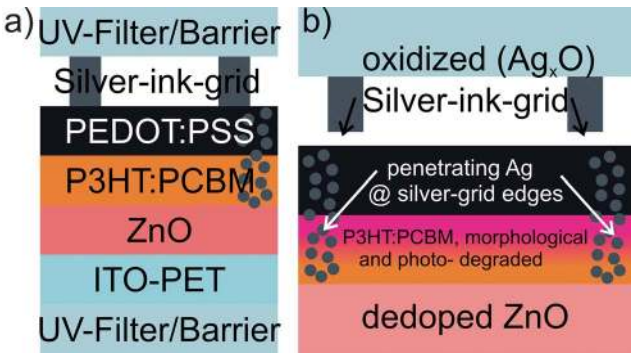

Fig. 33 Device structure (a) and degradation mechanism (b) of the RisøP solar cells as determined by imaging characterization. Already from the beginning of the study some local shunting of the device was observed. Besides a blocking layer formation due to oxidation of the silver–PEDOT:PSS interface or a dedoping of the ZnO, more shunts were observed at places of increased electric fields at the final stage of the degradation. A morphological change respectively degradation is assigned to the increase of the series resistance of the device, whereas the current decrease is assigned to active layer photo-oxidation.

the PEDTOS:PSS[36–38] or by an oxygen enhanced dedoping of the ZnO contact,[31,39] even though the state of doping at the ZnO–ITO interface was aspired by light soaking of the device previous to all characterizations. This might explain the increase in series resistance continuing until the final characterization (*T*00). Another possibility for the series resistance increase originates from unstable bulk heterojunction morphology. In view of the—except for the active layer—identically prepared RisøS devices (see next section), this appears to be the more probable explanation, since for RisøS devices no increase in series resistance was observed. Shunting is reflected within the *IV*-characteristics by increasingly negative currents under reverse voltage. The continuous decrease in photocurrent is likely due to homogeneous photo-degradation of the active layer. Oxygen penetration into these solar cells appears more probable due to the flexible barriers as compared to devices on glass.

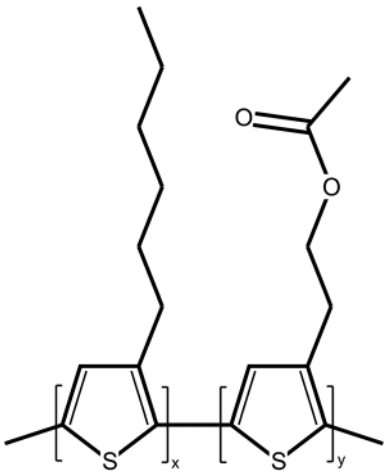

Fig. 34 Chemical structure of P3HT-*co*-P3AcET, used for the RisøS solar cell device.

Fig. 33 summarizes the acting degradation mechanisms present in the RisøP device: already at its initial characterization a number of shunts were detected by DLIT (a). The number of shunts increased further for longer operation times (Fig. 31c and d), driven by electro-migration of the silver at places of electric-field enhancements. Silver oxidation or ZnO dedoping leads to slight blocking contact features, as visible for the intermediate degradation state (see Fig. 32 for comparison). Finally, the increase in series resistance has to be assigned to a change in the active layer morphology in direct comparison with the RisøS device degradation.

3.2.7 P3HT-*co*-P3AcET:PCBM solution processed device on PET—RisøS. The flexible encapsulated solution processed RisøS solar cell exhibits the identical device structure as the RisøP cell. The only difference is found in the photoactive layer: RisøS exhibits a P3HT-based thiophene backbone copolymer: poly-3-hexylthiophene-*co*-3-(2-acetoxyethyl)thiophene (P3HT-*co*-P3AcET), see Fig. 34.

This has quite remarkable consequences for the resulting degradation mechanism: practically no series resistance increase is observed in the *IV*-characteristics. Only the formation of a blocking contact and a reduction of the photocurrent reflect the degradation behavior. The blocking contact is likely due to the oxidation of the silver–PEDOT:PSS interface[36–38] (compare with Fig. 36) or a dedoping of the electron collecting ZnO-contact by oxygen.[31,39] The reduction of the photocurrent could be assigned to a homogeneous photo-oxidation of the photoactive layer. In fact, DLIT does not reveal any further features, but proves that no shunts occur in combination with this active layer (Fig. 35). Hence the slightly better stability of RisøS over RisøP observed within the cycle experiment can be assigned to the improved morphological stability and possibly higher density of the photoactive layer. In the case of the RisøS device all imaging techniques can only confirm that no inhomogeneous degradation is acting on the device, all other conclusions have to be drawn on the basis of the *IV*-characteristics (Fig. 36).

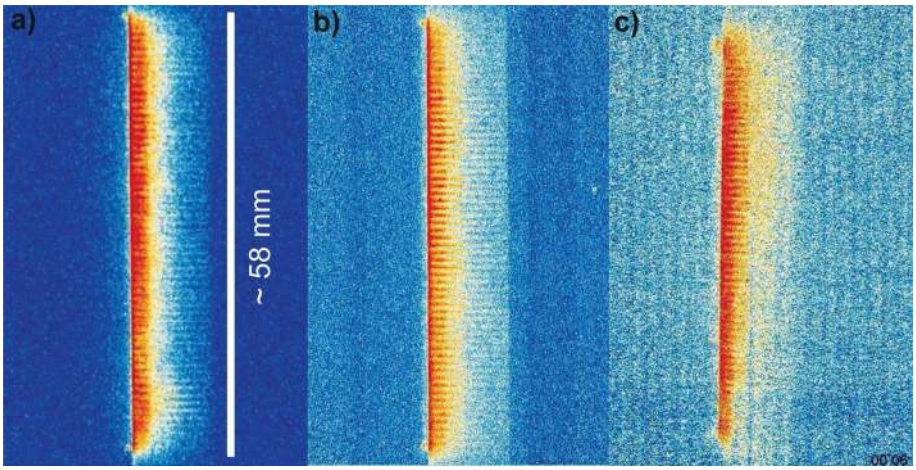

Fig. 35 DLIT characterization of the RisøS solar cell from the cycle experiment: initially at nominal *T*100 (a), after 42 hours at *T*44 (b) and after total 637 hours under full sun simulation at *T*03 (c). Forward excitation was done at +1.5 Volts. Under reverse excitation DLIT reveals no shunting features (not shown here).

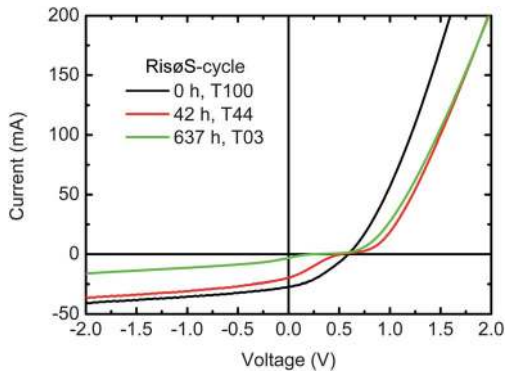

Fig. 36 *IV*-characteristics of the RisøS cycle device at initial (*T*100), after 42 hours (*T*44) and after total 637 hours (*T*03) under full sun illumination. After 42 hours stressing, the device loses part of the photocurrent and reveals a blocking contact respectively counter diode feature. After 637 hours of stressing the *IV*-curve exhibits a further developed blocking contact, causing final failure of the device. The active cell area of this device is 4.9 cm^2.

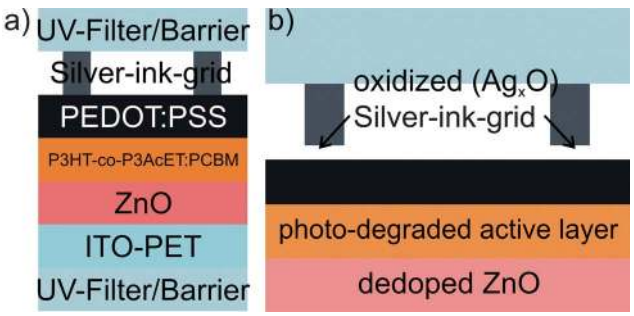

Fig. 37 Device structure (a) and degradation mechanism (b) of the RisøS solar cells. As derived from the *IV*-characterization, a blocking layer formation—assigned to either silver-oxide or dedoped ZnO—and a homogeneous photo-degradation of the active layer were the most likely degradation mechanism.

Fig. 37 depicts the most probable degradation mechanism of the RisøS device schematically. Silver oxidation on top of the fairly thick PEDOT:PSS interlayer and/or oxygen dedoping of the ZnO-interlayer results in the formation of a blocking contact. A general loss in photocurrent may be due to photo-degradation of the active layer. Interestingly the series resistance is not changed, which has to be assigned to a more stable bulk heterojunction morphology within the photoactive layer.

An increase in series resistance is clearly observed for the IMEC, NREL and ISE processed devices as well. In view of the Risø solar cell comparison between P and S type of devices, we have to include the possibility that these series resistance increases could be generally assigned to a morphological change, respectively morphological degradation of the active layer. Whereas this does not influence on the major degradation observed for the IMEC and the NREL device, the ISE degradation could be possibly dominated by these morphological changes as well. However, a series resistance increase within the photoactive layer would rather result in a better distributed current collection in the case of LBIC and current injection in the case of DLIT and ELI, which was not observed for the ISE device.

It should be briefly stated that neither *IV*-characterization nor the imaging techniques applied can discriminate between a metal oxide formation and a dedoping of ZnO interlayers. Both degradation mechanisms are controlled by oxygen and result in the formation of a blocking contact feature. More detailed investigations are required to distinguish between those potential degradation pathways relevant for the inverted type solar cell architectures.

4. Conclusion

In summary, the combined investigation of organic photovoltaic device degradation by accelerated aging under full sun illumination at elevated temperatures, *IV*-characterization and application of several imaging methods provides plenty of conclusive information about the predominant degradation paths. Notably, the intensity and spectrum of the soaking light are not the only crucial stressing parameters, but also the device temperature

reached under illumination can initiate additional degradation routes.

Of course the imaging information and the *IV*-characteristics reveal the degradation mechanisms not directly and an interpretation of the results based on existing knowledge is required. For example it is well-known that the lower work function electrode is most sensitive to oxidation and that sources for oxidizing agents are to be found in water and oxygen ingress through pinholes. Therefore background information has to be included within this analysis to obtain plausible explanations. However, the main advantage of imaging the degradation is found in the additional lateral information provided by the spatial resolution of device behavior.

This study revealed furthermore that more complicated degradation features can only be understood by the application of more than one or even all imaging methods applied within this study. The large set of photovoltaic devices produced by several labs and differing in various aspects provided a fundamental basis for gaining improved knowledge over the dominant routes of degradation. The main degradation mechanisms observed are: (i) oxidation of aluminium, (ii) blocking contact formation (due to silver oxidation or ZnO-dedoping), (iii) electro-migration of silver especially at edge enhanced electric fields, (iv) water and oxygen ingress through pinholes and from the edges of the solar cell, and (v) water release from especially the highly conductive version of PEDOT:PSS. Only for flexible devices significant degradation due to photo-oxidation and morphological changes of the active layer were observed. Thus at present the organic photovoltaic device stability is mostly controlled by the instability of the charge collecting electrodes, which is in contrast to the common belief that the organic semiconductors themselves constitute the weak part of the device.

This study reveals furthermore device stabilization effects achieved by (i) prevention of "naked" aluminium–active layer interfaces, (ii) inhibition of silver electro-migration and (iii) the use of metal-oxide charge extracting interlayers.

The degradation mechanisms detected here should ultimately be supported and confirmed by elemental analysis, which is beyond the scope of this study and will be the topic of a future report on the same set of devices investigated within this cooperation.

In conclusion, we believe the comprehensive investigation of device aging by imaging characterization presented within this study has considerably advanced the understanding of the OPV community on degradation and constructive stabilization of organic solar cells.

Acknowledgements

RR, MS, MB and HH are grateful for financial support from the Thuringian Ministry of Culture and the German Federal Ministry of Education and Research in the frameworks of FIPV II and PPP (contract number 13N9843), respectively. This work has been supported by the Danish Strategic Research Council (2104-07-0022), EUDP (j.no. 64009-0050) and the Danish National Research Foundation. Partial financial support was also received from the European Commission as part of the Framework 7 ICT 2009 collaborative project HIFLEX (grant no. 248678), partial financial support from the EUIndian framework of the "Largecells" project that received funding from the European Commission's Seventh Framework Programme (FP7/2007–2013. grant no. 261936), partial financial support was also received from the European Commission as part of the Framework 7 ICT 2009 collaborative project ROTROT (grant no. 288565) and from PVERA-NET (project acronym POLYSTAR). To the Spanish Ministry of Science and Innovation, MICINN-FEDER project ENE2008-04373, to the Consolider NANOSELECT project CSD2007-00041, to the Xarxa de Referència en Materials Avançats per a l'Energia, XaRMAE of the Catalonia Government (Spain). To CONACYT (México) for the PhD scholarship awarded to GT-E. DMT acknowledges support from the Inger and Jens Bruun Foundation through The American–Scandinavian Foundation.

References

1 P. W. M. Blom, V. D. Mihailetchi, L. J. A. Koster and D. E. Markov, *Adv. Mater.*, 2007, **19**, 1551–1566.
2 P. L. T. Boudreault, A. Najari and M. Leclerc, *Chem. Mater.*, 2011, **23**, 456–469.
3 J. D. Servaites, M. A. Ratner and T. J. Marks, *Energy Environ. Sci.*, 2011, **4**, 4410–4422.
4 F. C. Krebs, *Sol. Energy Mater. Sol. Cells*, 2009, **93**, 394–412.
5 T. D. Nielsen, C. Cruickshank, S. Foged, J. Thorsen and F. C. Krebs, *Sol. Energy Mater. Sol. Cells*, 2010, **94**, 1553–1571.
6 M. A. Green, K. Emery, Y. Hishikawa, W. Warta and E. D. Dunlop, *Prog. Photovoltaics*, 2011, **19**, 565–572.
7 R. F. Service, *Science*, 2011, **332**, 293.
8 M. Jørgensen, K. Norrman and F. C. Krebs, *Sol. Energy Mater. Sol. Cells*, 2008, **92**, 686–714.
9 A. Seemann, T. Sauermann, C. Lungenschmied, O. Armbruster, S. Bauer, H. J. Egelhaaf and J. Hauch, *Sol. Energy*, 2011, **85**, 1238–1249.
10 M. T. Lloyd, C. H. Peters, A. Garcia, I. V. Kauvar, J. J. Berry, M. O. Reese, M. D. McGehee, D. S. Ginley and D. C. Olson, *Sol. Energy Mater. Sol. Cells*, 2011, **95**, 1382–1388.
11 D. M. Tanenbaum, H. F. Dam, R. Rösch, M. Jørgensen, H. Hoppe and F. C. Krebs, *Sol. Energy Mater. Sol. Cells*, 2012, **97**, 157–170.
12 M. Seeland, R. Rosch and H. Hoppe, *J. Appl. Phys.*, 2011, **109**, 064513.
13 F. C. Krebs, S. A. Gevorgyan and J. Alstrup, *J. Mater. Chem.*, 2009, **19**, 5442–5451.
14 M. O. Reese, S. A. Gevorgyan, M. Jorgensen, E. Bundgaard, S. R. Kurtz, D. S. Ginley, D. C. Olson, M. T. Lloyd, P. Moryillo, E. A. Katz, A. Elschner, O. Haillant, T. R. Currier, V. Shrotriya, M. Hermenau, M. Riede, K. R. Kirov, G. Trimmel, T. Rath, O. Inganas, F. L. Zhang, M. Andersson, K. Tvingstedt, M. Lira-Cantu, D. Laird, C. McGuiness, S. Gowrisanker, M. Pannone, M. Xiao, J. Hauch, R. Steim, D. M. DeLongchamp, R. Rosch, H. Hoppe, N. Espinosa, A. Urbina, G. Yaman-Uzunoglu, J. B. Bonekamp, A. van Breemen, C. Girotto, E. Voroshazi and F. C. Krebs, *Sol. Energy Mater. Sol. Cells*, 2011, **95**, 1253–1267.
15 D. M. Tanenbaum, M. Hermenau, E. Voroshazi, M. T. Lloyd, Y. Galagan, B. Zimmermann, M. Hösel, H. F. Dam, M. Jørgensen, S. A. Gevorgyan, S. Kudret, W. Maes, L. Lutsen, D. Vanderzande, U. Würfel, R. Andriessen, R. Rösch, H. Hoppe, G. Teran-Escobar, M. Lira-Cantu, A. Rivaton, G. Y. Uzunoğlu, D. Germack, B. Andreasen, M. V. Madsen, K. Norrman and F. C. Krebs, *RSC Adv.*, 2012, **2**, 882–893.
16 J. M. Kroon, M. M. Wienk, W. J. H. Verhees and J. C. Hummelen, *Thin Solid Films*, 2002, **403**, 223–228.
17 T. Jeranko, H. Tributsch, N. S. Sariciftci and J. C. Hummelen, *Sol. Energy Mater. Sol. Cells*, 2004, **83**, 247–262.
18 M. Seeland, R. Rösch and H. Hoppe, Imaging Techniques for Studying OPV Stability and Degradation in *Stability and Degradation of Organic and Polymer Solar Cells*, ed. F. C. Krebs, Wiley, 2012, ISBN: 978-1-119-95251-0.
19 F. C. Krebs, R. Søndergaard and M. Jørgensen, *Sol. Energy Mater. Sol. Cells*, 2011, **95**, 1348–1353.

20 K. Tvingstedt, K. Vandewal, A. Gadisa, F. L. Zhang, J. Manca and O. Inganas, *J. Am. Chem. Soc.*, 2009, **131**, 11819–11824.
21 K. Vandewal, K. Tvingstedt, A. Gadisa, O. Inganas and J. V. Manca, *Nat. Mater.*, 2009, **8**, 904–909.
22 M. Seeland, R. Rösch and H. Hoppe, *J. Appl. Phys.*, 2012, **111**, 024505.
23 O. Breitenstein and M. Langenkamp, Lock-in Thermography - Basics and Use for Functional Diagnostics of Electronic Components, Springer, 2003, ISBN: 3-540-43439-9.
24 M. Hermenau, M. Riede, K. Leo, S. A. Gevorgyan, F. C. Krebs and K. Norrman, *Sol. Energy Mater. Sol. Cells*, 2011, **95**, 1268–1277.
25 H. Hoppe, J. Bachmann, B. Muhsin, K. H. Drue, I. Riedel, G. Gobsch, C. Buerhop-Lutz, C. J. Brabec and V. Dyakonov, *J. Appl. Phys.*, 2010, **107**, 014505.
26 J. Bachmann, C. Buerhop-Lutz, C. Deibel, I. Riedel, H. Hoppe, C. J. Brabec and V. Dyakonov, *Sol. Energy Mater. Sol. Cells*, 2010, **94**, 642–647.
27 E. Voroshazi, B. Verreet, A. Buri, R. Muller, D. Di Nuzzo and P. Heremans, *Org. Electron.*, 2011, **12**, 736–744.
28 J. Alstrup, M. Jørgensen, A. J. Medford and F. C. Krebs, *ACS Appl. Mater. Interfaces*, 2010, **2**, 2819–2827.
29 R. Rösch, F. C. Krebs, D. M. Tanenbaum and H. Hoppe, *Sol. Energy Mater. Sol. Cells*, 2012, **97**, 176–180.
30 B. Zimmermann, U. Wurfel and M. Niggemann, *Sol. Energy Mater. Sol. Cells*, 2009, **93**, 491–496.
31 M. R. Lilliedal, A. J. Medford, M. V. Madsen, K. Norrman and F. C. Krebs, *Sol. Energy Mater. Sol. Cells*, 2010, **94**, 2018–2031.
32 K. Norrman, N. B. Larsen and F. C. Krebs, *Sol. Energy Mater. Sol. Cells*, 2006, **90**, 2793–2814.
33 Y. Galagan, J. Rubingh, R. Andriessen, C. C. Fan, P. W. M. Blom, S. C. Veenstra and J. M. Kroon, *Sol. Energy Mater. Sol. Cells*, 2011, **95**, 1339–1343.
34 M. Seeland, R. Rösch, B. Muhsin, G. Gobsch and H. Hoppe, *Energy Procedia*, 2011, in press.
35 A. Elschner, *Sol. Energy Mater. Sol. Cells*, 2011, **95**, 1333–1338.
36 M. S. White, D. C. Olson, S. E. Shaheen, N. Kopidakis and D. S. Ginley, *Appl. Phys. Lett.*, 2006, **89**, 143517.
37 S. K. Hau, H. L. Yip, N. S. Baek, J. Y. Zou, K. O'Malley and A. K. Y. Jen, *Appl. Phys. Lett.*, 2008, **92**, 253301.
38 J. B. Kim, C. S. Kim, Y. S. Kim and Y. L. Loo, *Appl. Phys. Lett.*, 2009, **95**, 183301.
39 W. J. E. Beek, M. M. Wienk, M. Kemerink, X. N. Yang and R. A. J. Janssen, *J. Phys. Chem. B*, 2005, **109**, 9505–9516.